

# Asymptotic scaling theory of electrostatic turbulent transport in magnetised fusion plasmas

T. Adkins\* and F. I. Parra

*Princeton Plasma Physics Laboratory, Princeton, New Jersey, 08540, USA*

I. G. Abel

*Department of Physics, University of Maryland, College Park, Maryland, 20742, USA*

M. Barnes and A. A. Schekochihin

*Rudolf Peierls Centre for Theoretical Physics, University of Oxford, Oxford, OX1 3PU, UK*

S. Buller

*Department of Astrophysical Sciences, Princeton University, Princeton, New Jersey, 08543, USA*

W. Dorland†

*Department of Physics, University of Maryland, College Park, Maryland, 20742, USA and*

*Institute for Research in Electronics and Applied Physics,*

*Energy Research Facility, 8279 Paint Branch Drive, College Park, MD 20742*

P. G. Ivanov

*United Kingdom Atomic Energy Authority, Culham Campus, Abingdon, OX14 3DB, UK*

R. Meyrand

*Department of Physics & Astronomy, University of New Hampshire, Durham, New Hampshire, 03824, USA*

J. Squire

*Department of Physics, University of Otago, Dunedin, 9016, New Zealand*

(Dated: January 23, 2026)

Turbulent transport remains one of the principal obstacles to achieving efficient magnetic confinement in fusion devices. Two of the dominant drivers of the turbulence are microscale instabilities fuelled by electron- and ion-temperature gradients (ETG and ITG), whose nonlinear saturation determines the cross-field transport of particles and energy. Despite decades of study, predictive modelling of this turbulence has been limited either to expensive gyrokinetic simulations or to reduced models calibrated by fitting to numerical or experimental data, restricting their utility for reactor design. Here we present a simple asymptotic scaling theory that unifies ETG- and ITG-driven turbulence within a common framework. By balancing the fundamental time scales of linear growth, nonlinear decorrelation, and parallel propagation, the theory isolates the dependence of the heat flux on equilibrium parameters to two key quantities: the parallel system scale and the outer-scale aspect ratio. We show that these quantities encapsulate the essential physics of saturation, leading to distinct predictions for ETG and ITG transport: a cubic scaling with the temperature gradient in the electron channel, and a linear scaling in the ion channel. Extensive nonlinear gyrokinetic simulations confirm that these theoretical predictions hold irrespective of the magnetic geometry (slab, tokamak, or stellarator), including the first numerical confirmation of the cubic ETG scaling anticipated by earlier theory. The result is a reduced yet interpretable model of turbulent transport, grounded in first principles while simultaneously simple enough to guide the design of future fusion devices. By isolating the dependence on just the parallel system scale and the outer-scale aspect ratio, our framework provides a physics-based foundation for fast, geometry-aware transport models, offering a pathway toward reactor optimisation in both tokamaks and stellarators.

## I. INTRODUCTION

Magnetic-confinement-fusion devices such as tokamaks and stellarators aim to sustain plasmas at temperatures and densities high enough for the energy produced by fusion reactions to outpace the losses. The dominant source of these

\* [tadkins@pppl.gov](mailto:tadkins@pppl.gov)

† Deceased Sept. 22, 2024

losses comes from turbulence — a chaotic, nonlinear ensemble of Larmor-scale fluctuations driven by the gradients of the plasma density and temperature — that transports particles and heat across the confining magnetic field. Since the overall power balance, and thus viability, of the device is governed by this turbulent transport, the design of future fusion reactors needs reliable, predictive, physics-based models that connect the parameters of the plasma and magnetic equilibria to the resulting turbulent fluxes of particle and energy. Today's most accurate tool, first-principles gyrokinetic simulations [1–7], are computationally intensive, while widely used reduced models (e.g., TGLF [8, 9] or QuaLiKiz [10, 11]) rely on closures and fits that limit extrapolation to the novel parameter regimes that future fusion reactors will inhabit. This motivates a complementary approach: the development of simple yet fundamental scaling theories that distil the essential mechanisms that determine the steady-state turbulent transport, thereby providing reliable guidance for reactor design.

Much of the focus of current research is on the turbulence driven by electrostatic instabilities associated with either the electron-temperature gradient (ETG) [12–15] or the ion-temperature gradient (ITG) [16–18], which typically live on scales comparable to the electron and ion Larmor radii, respectively. Though it has been long understood that ITG-driven turbulence typically dominates core transport (see references cited above), ETG-driven turbulence can become significant when ion-scale modes become suppressed by, e.g., strong  $\mathbf{E} \times \mathbf{B}$  shear in the steep-gradient regions of a tokamak (e.g., the pedestal), particularly in spherical or low-aspect-ratio configurations [see 19–23, and references therein]. As such, developing a better understanding of the turbulent transport driven by both ETG and ITG is a key ingredient in the successful design of future reactors. Despite their similarity in terms of linear physics, however, previous theoretical [24–26] and experimental [27] studies suggest that the nonlinear saturation of ETG and ITG can differ significantly, meaning that the resulting transport levels and their scaling with equilibrium parameters certainly cannot be inferred from linear theory alone. Understanding these distinct saturation pathways is, however, essential for constructing reduced, predictive models of turbulent transport.

In this paper, we develop an asymptotic scaling theory for the dependence of both ETG- and ITG-driven turbulent transport on parameters of the plasma equilibrium and the magnetic geometry when driven far above marginality. The final scaling estimates arise from a simple competition between three fundamental timescales associated with gyrokinetic fluctuations: the rates of linear growth, nonlinear decorrelation, and parallel propagation (along the magnetic field). This balance reduces the problem to determining two key quantities: the parallel system scale  $L_{\parallel}$  and the perpendicular aspect ratio of the most energetic ('outer-scale') fluctuations  $\mathcal{A}^o$  (defined here as the ratio of their characteristic radial wavenumber to their binormal one). The former is effectively a measure of the parallel correlation length of the turbulence, and is typically determined by the geometry of the confining field. Crucially, the outer-scale aspect ratio is set by the nature of the adiabatic response of the non-driving species, leading to fundamentally different predictions for ETG- and ITG-driven turbulence. In particular, we show that while the modified adiabatic electron response causes  $\mathcal{A}^o$  to scale linearly with the ion-temperature gradient [26], the unmodified adiabatic ion response on electron scales leads to  $\mathcal{A}^o$  being independent of equilibrium parameters for the ETG case. This results in ETG-driven turbulence displaying significantly stiffer transport [28] than its ITG counterpart, the turbulent heat flux scaling cubically with the temperature gradient, as opposed to linearly for ITG. This scaling theory is verified against extensive nonlinear gyrokinetic simulations in straight, axisymmetric, and non-axisymmetric magnetic-field geometries, showing remarkable agreement with the numerical results, which also represent the first confirmation of the cubic ETG scaling with the temperature gradient, as predicted by previous theoretical studies [25, 29, 30]. By distilling the nonlinear saturation physics of ITG and ETG turbulence down to the two parameters  $L_{\parallel}$  and  $\mathcal{A}^o$ , our approach unifies both regimes within a single theoretical framework. The result is a reduced but interpretable theory that captures the correct asymptotic scalings, providing a physics-based foundation for predictive models. Such models are particularly valuable in reactor design and stellarator optimisation, where scanning across large spaces of magnetic geometries and equilibrium profiles demands fast yet reliable tools informed by first-principles theory.

The remainder of this paper is organised as follows. In §II, we present the asymptotic scaling theory that is the focus of this paper, deriving predictions for the scaling of the heat flux in ETG- and ITG-driven turbulence from a simple balance of timescales. Its implications for slab (§III), axisymmetric (§IV), and non-axisymmetric (§V) geometries are then considered, with the predictions tested, successfully, by a vast array of numerical simulations. We summarise our findings in §VI and discuss various lines of investigation left open by this work in §VII. Technical details of the numerical simulations are given in §A, alongside supplementary data in §B.

## II. ASYMPTOTIC SCALING THEORY

In this section, we develop the theoretical framework wherein we derive the asymptotic scaling theory for the dependence of the turbulent transport on equilibrium parameters. After introducing electrostatic gyrokinetics (§II A) and the local flux-tube limit (§II B), we consider the various time scales appearing in the gyrokinetic equation (§II C) before demonstrating how straightforward physical arguments about the nature of the competition between these

time scales can be leveraged to determine the properties of the saturated state (sections II D to II F). Note that throughout §II, we consider turbulence in plasma models containing a single kinetic species (either electrons or ions). The multi-species dynamics that can arise when electron- and ion-scale fluctuations are coupled are discussed further in §VII B. In §II G, we also highlight the contrasting adiabatic responses seen on electron and ion scales, since these differences are responsible for the distinct saturation physics of ETG and ITG turbulence.

### A. Electrostatic gyrokinetics

We consider magnetised-plasma turbulence driven by gradients in the equilibrium density  $n_s$  and temperature  $T_s$  of species  $s$  in the presence of a mean magnetic field  $\mathbf{B}$ . The turbulent fluctuations are assumed to satisfy the usual gyrokinetic ordering [1–3]:

$$k_{\perp}\rho_s \sim k_{\parallel}L \sim 1, \quad \frac{\omega}{\Omega_s} \sim \frac{\rho_s}{L} \equiv \rho_{*s} \ll 1, \quad (1)$$

where  $k_{\perp}$  and  $k_{\parallel}$  are characteristic wavenumbers perpendicular and parallel to  $\mathbf{b} = \mathbf{B}/|\mathbf{B}|$ , respectively,  $\rho_s$  and  $\Omega_s$  are the Larmor radius and frequency of species  $s$ ,  $\omega$  is the inverse time scale associated with the fluctuations, and  $L$  is some characteristic length scale of variation of the plasma equilibrium (e.g., of  $n_s$ ,  $T_s$ , or  $\mathbf{B}$ ). We assume that there exist well-defined flux-surfaces labelled by  $\psi$  (later taken to be either the poloidal or toroidal flux), allowing us to write the mean magnetic field in Clebsch form  $\mathbf{B} = \nabla\alpha \times \nabla\psi$ , with  $\alpha$  the field-line label. In this case, it can be shown that, in the absence of sonic flows [2], the plasma equilibrium is, to lowest order in  $\rho_{*s}$ , a function only of  $\psi$ , viz.,  $n_s = n_s(\psi)$  and  $T_s = T_s(\psi)$ . Given that these equilibrium quantities evolve on a slow transport time scale  $\tau_E \sim \rho_{*s}^2\omega$ , we treat them as constant over the time scales of the turbulent fluctuations. Note that while we will not consider the effects of any equilibrium flows in our analysis (neglecting, in particular, both equilibrium flow shear and finite-Mach-number rotational drifts), interested readers may find a prescription for modifying our findings in the presence of flowshear in, e.g., [31].

If the plasma beta  $\beta_s = 8\pi n_s T_s / B^2$  is sufficiently small for fluctuations in the magnetic field to be neglected — we refer to this as the electrostatic limit — the only electromagnetic field that participates in the dynamics is the perturbed electrostatic potential  $\delta\phi$ . Then, the non-adiabatic distribution function  $h_s = h_s(\mathbf{R}_s, \varepsilon_s, \mu_s, t)$ , related to the perturbed distribution function by  $\delta f_s = -(Z_s e \delta\phi / T_s) F_s + h_s$ , evolves according to the gyrokinetic equation [1–3]:

$$\frac{\partial}{\partial t} \left( h_s - \frac{Z_s e \langle \delta\phi \rangle_{\mathbf{R}_s}}{T_s} F_s \right) + (v_{\parallel} \mathbf{b} + \mathbf{v}_{ds} + \langle \mathbf{v}_E \rangle_{\mathbf{R}_s}) \cdot \nabla h_s + \langle \mathbf{v}_E \rangle_{\mathbf{R}_s} \cdot \nabla F_s = \sum_{s'} \langle C_{ss'} \rangle_{\mathbf{R}_s}, \quad (2)$$

in which  $\mathbf{R}_s = \mathbf{r} - \mathbf{b} \times \mathbf{v}/\Omega_s$  is the gyrocentre position,  $\varepsilon_s = m_s v^2/2$  is the particle kinetic energy,  $\mu_s = m_s v_{\perp}^2/2B$  is the magnetic moment,  $Z_s e$  and  $F_s$  are the charge and equilibrium Maxwellian distribution of species  $s$ ,  $\mathbf{v}_{ds} = (\mathbf{b}/2\Omega_s) \times (2v_{\parallel}^2 \mathbf{b} \cdot \nabla \mathbf{b} + v_{\perp}^2 \nabla \log B)$  are the magnetic drifts,  $\mathbf{v}_E = (c/B) \mathbf{b} \times \nabla \delta\phi$  is the perturbed  $\mathbf{E} \times \mathbf{B}$  drift, and  $\langle \dots \rangle_{\mathbf{R}_s}$  is the standard gyroaverage at constant gyrocentre position. The term on the right-hand side is the operator encoding the effect of collisions between species  $s$  and  $s'$  on  $h_s$ . Throughout this paper, we will be concerned with collisionless (or nearly collisionless) dynamics, and so we need not quote a specific form of the collision operator here. The electrostatic gyrokinetic equation (2) is closed by the quasineutrality condition

$$\sum_s \frac{(Z_s e)^2 n_s}{T_s} \delta\phi = \sum_s Z_s e \int d^3 \mathbf{v} \langle h_s \rangle_{\mathbf{r}}, \quad (3)$$

where  $\langle \dots \rangle_{\mathbf{r}}$  denotes the gyroaverage at constant particle position  $\mathbf{r}$ .

### B. Local flux-tube limit

In what follows, we restrict our consideration to the local limit, in that the dynamics supported by (2) will be integrated in a ‘flux tube’: a field-line-following domain of perpendicular size that is infinitesimal in comparison to the length scales associated with the plasma equilibrium  $F_s$  and the equilibrium magnetic field  $\mathbf{B}$ . We adopt a set of coordinates  $(x, y, z)$ , in which  $z$  is the coordinate along the magnetic field, while  $x \propto \psi$  and  $y \propto \alpha$  are the radial and binormal coordinates, respectively, with suitable normalisations such that they have units of length and that  $\mathbf{B} = B_0 \nabla x \times \nabla y$ , with  $B_0$  some normalising magnetic field. Note that  $x$  and  $y$  are not in general orthogonal to one another, viz.,  $\nabla x \cdot \nabla y \neq 0$ . In what follows, we will give the exact definitions of these coordinates in terms of usual

toroidal coordinates where appropriate. Perpendicular gradients associated with the equilibrium, such as the density and temperature gradients

$$\frac{1}{L_{n_s}} \equiv -\frac{d \ln n_s}{dx}, \quad \frac{1}{L_{T_s}} \equiv -\frac{d \ln T_s}{dx}, \quad (4)$$

are assumed constant across the domain and equal to their value at the centre of the flux tube [32]. Periodic boundary conditions are imposed in the plane perpendicular to the equilibrium magnetic field, allowing any fluctuating quantity to be expressed in terms of its Fourier amplitudes for the perpendicular wavenumber  $\mathbf{k}_\perp = k_x \nabla x + k_y \nabla y$ , viz.,

$$h_s(\mathbf{R}_s, \varepsilon_s, \mu_s, t) = \sum_{\mathbf{k}_\perp} e^{i\mathbf{k}_\perp \cdot \mathbf{R}_s} h_{s\mathbf{k}_\perp}(z, \varepsilon_s, \mu_s, t), \quad \delta\phi(\mathbf{r}, t) = \sum_{\mathbf{k}_\perp} e^{i\mathbf{k}_\perp \cdot \mathbf{r}} \delta\phi_{\mathbf{k}_\perp}(z, t). \quad (5)$$

Throughout this paper, the scalar measure of the turbulent transport that will be our focus is the radial turbulent heat (energy) flux of species  $s$ , which can be expressed as

$$Q_s = \left\langle \int d^3 \mathbf{v} \varepsilon_s \langle h_s(\mathbf{v}_E \cdot \nabla x) \rangle_{\mathbf{r}} \right\rangle_{x,y,z}. \quad (6)$$

In (6), the angle brackets denote an average over full spatial domain, with the average over  $z$  including a factor of the Jacobian  $[(\nabla x \times \nabla y) \cdot \nabla z]^{-1}$  (see, e.g., appendix A of [33]). While gyrokinetic turbulence can, and often does, support a particle flux  $\Gamma_s$ , we assume that the turbulence is sufficiently strongly driven that the heat flux dominates over the particle flux,  $Q_s/T_s \gg \Gamma_s$ ; indeed, in the single-particle-species simulations that we will consider,  $\Gamma_s$  is identically zero because of the Boltzmann density response of the non-kinetic species. In terms of equilibrium parameters, this generally corresponds to the limit of  $\eta_s \equiv L_{n_s}/L_{T_s} \gg 1$ . By focussing on this strongly-driven limit, we are able to construct a theory of the turbulence that is independent of the particular details of system-specific linear (or nonlinear) thresholds, returning to the question of how it connects to the near-marginal regime (wherein  $Q_s/T_s \sim \Gamma_s$ ) in §VII A.

### C. Linear and nonlinear time scales

As in studies of magnetised plasma turbulence in other contexts (see, e.g., [34] and references therein), progress towards understanding the turbulence supported by the gyrokinetic equation (2) can be made by considering the various linear and nonlinear time scales contained therein. For our purposes here, there are three important time scales to consider:

1. Linear growth rate: Linear instabilities are the mechanism by which free energy is extracted from the equilibrium gradients in  $n_s$  and  $T_s$ , the resulting fluctuations then processed by the turbulence to support a heat flux. At each binormal scale  $k_y$ , there will exist a family of unstable modes parametrised by  $k_x$  (and by  $k_\parallel$  in the straight-field case, for which the parallel structure is well-described by a discrete set of Fourier modes). The growth rate most relevant for turbulence saturation will be the one maximised over all  $k_x$  (or  $k_\parallel$ ), which we denote  $\gamma_{k_y}$ . At this stage, we remain agnostic as to the precise nature of the underlying instability, simply regarding  $\gamma_{k_y}$  as the effective rate at which energy is injected into the turbulence.
2. Nonlinear decorrelation rate: The time scale of the nonlinear interactions appearing in (2) is simply the rate at which fluctuations are sheared by the perturbed  $\mathbf{E} \times \mathbf{B}$  flow, viz.,

$$t_{nl}^{-1} \sim k_\perp v_E \sim \frac{c}{B} k_x k_y \delta\phi_{k_y}. \quad (7)$$

Here, and in what follows,  $\delta\phi_{k_y}$  refers to the characteristic amplitude of the electrostatic potential at the binormal scale  $k_y$ , rather than to the Fourier transform of the field. While a precise definition of  $\delta\phi_{k_y}$  is not important since the phenomenological theory that is to follow predicts only scalings, it could be formally defined in terms of an integral over squared Fourier amplitudes (see, e.g., equation (3.3) of [31]), or via a second-order structure function (see, e.g., [35]). The radial scale  $k_x$  appearing in (7) is an implicit function of  $k_y$ , viz., at each  $k_y$ , the turbulent fluctuations have a typical radial scale  $k_x$  that depends on  $k_y$ . Following [31], we define the *fluctuation aspect ratio* at the scale  $k_y$  as  $\mathcal{A} \equiv k_x/k_y$ , allowing us to rewrite the nonlinear rate (7) as

$$t_{nl}^{-1} \sim \Omega_s \mathcal{A} (k_y \rho_s)^2 \delta\phi_{k_y}. \quad (8)$$

The presence of  $\mathcal{A}$  in (8) will turn out to be crucial in determining the difference in scaling of the heat flux between ETG- and ITG-driven turbulence (see §IV). Note that we are implicitly assuming that the  $k_x$  appearing in  $\mathcal{A}$  is evaluated at the location in  $z$  at which the heat flux is maximal (e.g., the outboard midplane of a tokamak).

3. Parallel propagation rate: Though implicit in their definition, neither  $\gamma_{k_y}$  nor  $t_{\text{nl}}^{-1}$  contain any explicit information about the parallel scales of the turbulence, since both originate from terms in (2) involving only perpendicular gradients of the perturbed fields. This information enters instead through the *parallel propagation rate*  $\omega_{\parallel}$ , which represents the characteristic time associated with the parallel dynamics along the field lines. As with  $\gamma_{k_y}$ , we will for now remain agnostic as to the precise form of  $\omega_{\parallel}$ , but this additional time scale is nevertheless essential for understanding how the parallel dynamics participate in the turbulence.

There are, of course, a number of other time scales supported by (2) that we have not listed above, including, for example, the characteristic time scales associated with trapped particles or magnetic drifts (which we discuss further in §IV). For present purposes, however, we will find that the combination of the linear growth rate  $\gamma_{k_y}$ , the nonlinear decorrelation rate  $t_{\text{nl}}^{-1}$ , and the parallel propagation rate  $\omega_{\parallel}$  is sufficient to formulate a general theory for the asymptotic scaling of the heat flux (6).

#### D. Outer-scale dynamics

In order for the free energy extracted from the equilibrium gradients to give rise to a turbulent state, fluctuations driven by linear instabilities must survive long enough to interact nonlinearly. With this in mind, we define the *outer scale* to be the scale at which the rates of nonlinear decorrelation and linear injection balance [24, 25, 30]:

$$(t_{\text{nl}}^{-1})^{\text{o}} \sim \gamma_{k_y}^{\text{o}}. \quad (9)$$

Here, and in what follows, the superscript ‘o’ denotes quantities associated with the outer scale. The inevitability of the balance (9), assuming well-developed plasma turbulence, can be seen as follows. Suppose that the nonlinear rate were subdominant to the linear one at all binormal scales  $k_y$ , so that the system remained effectively linear. Then, amplitudes  $\delta\phi_{k_y}$  would grow exponentially until the nonlinear rate was at least as large as the linear one  $t_{\text{nl}}^{-1} \gtrsim \gamma_{k_y}$  at all unstable scales. However, the nonlinear rate cannot be strictly larger than the linear growth rate at all scales, as otherwise there would be no meaningful injection of energy into the turbulence, since the associated rapid decorrelation would disrupt the phase relationships between potential and distribution-function fluctuations required for linear growth. Thus, the existence of an outer scale defined by (9) is a consequence of saturated turbulence that is homogenous in time (i.e., not dominated by intermittent behaviour).

To estimate the heat flux  $Q_s$ , it will be useful to rewrite its definition (6) explicitly in terms of a sum over the Fourier components of the fluctuations, viz.,

$$Q_s = \sum_{\mathbf{k}_{\perp}} \langle Q_{s\mathbf{k}_{\perp}} \rangle_z, \quad Q_{s\mathbf{k}_{\perp}} \equiv \text{Im} \left[ \frac{ck_y}{B_0} \int d^3\mathbf{v} \varepsilon_s J_0(a_s) h_{s\mathbf{k}_{\perp}}^* \delta\phi_{\mathbf{k}_{\perp}} \right], \quad (10)$$

where  $J_0(a_s)$  is the zeroth-order Bessel function of the first kind,  $a_s = k_{\perp} v_{\perp} / \Omega_s$ , and ‘\*’ denotes the complex conjugate. Using quasineutrality (3) to estimate the non-adiabatic distribution function as  $h_s \sim (Z_s e \delta\phi / T_s) F_s$ , it is clear that the integral in (10) will be dominated by some outer scale  $k_y^{\text{o}} \rho_s \ll 1$  provided that the amplitudes of the fluctuations decay faster than  $k_y^{-1}$  at scales  $k_y > k_y^{\text{o}}$  — in the so-called ‘inertial range’ — a condition that is readily satisfied in our simulations (see figure 2 or §B). Note that we do not provide a detailed treatment of the inertial-range dynamics here, partly because these have been addressed in previous studies [24, 25, 30], but primarily because the scaling of the heat flux, the focus of this paper, is determined entirely by the outer-scale dynamics.

Assuming that the phase relationship between  $h_s$  and  $\delta\phi$  does not introduce any nontrivial factors, we estimate an upper bound for  $Q_s$  as follows:

$$Q_s \sim Q_s^{\text{o}} \sim n_s T_s v_{\text{th}s} k_y^{\text{o}} \rho_s \left( \frac{Z_s e \delta\phi_{k_y^{\text{o}}}}{T_s} \right)^2. \quad (11)$$

Using (8) and (9), the dependence of (11) on the outer-scale amplitude can be eliminated, yielding [cf. (3.8) of [31]]:

$$\frac{Q_s}{n_s T_s v_{\text{th}s}} \sim \left( \frac{\gamma_{k_y^0}}{\Omega_s} \right)^2 \frac{1}{(k_y^0 \rho_s)^3 (\mathcal{A}^0)^2}. \quad (12)$$

Up to this point, we have made no assumptions about the specific nature of the unstable modes, beyond requiring that the turbulence is strongly driven and that the temperature fluctuations are comparable to those in the electrostatic potential, *viz.*,  $\delta T_s/T_s \sim Z_s e \phi/T_s$ . To proceed further, we adopt a simple estimate of the growth rate of temperature-gradient-driven instabilities [cf. (2)],

$$\gamma_{k_y^0} \sim \left| \frac{\langle \mathbf{v}_E \rangle_{\mathbf{R}_s} \cdot \nabla F_s}{h_s} \right|_{k_y^0} \sim \eta_s \omega_{*s} \equiv \frac{k_y^0 \rho_s v_{\text{th}s}}{2 L_{T_s}}, \quad (13)$$

where, to obtain the final expression, we have once again used quasineutrality (3) to estimate  $h_s \sim (Z_s e \delta \phi/T_s) F_s$ . The estimate (13) is typical of both linear ETG- and ITG-driven electrostatic modes [24, 25], and should be viewed primarily as an estimate for the effective rate of energy injection, rather than the rate at which any individual perturbations grow linearly. Inspection of (12) makes it obvious that we then have two remaining unknowns at the outer scale: the binormal wavenumber  $k_y^0 \rho_s$  and aspect ratio  $\mathcal{A}^0$ . Let us first focus our attention on the former.

### E. Critical balance

Given that, at fixed  $\mathcal{A}^0$ , the heat flux scales inversely with the binormal wavenumber,  $Q_s \propto (k_y^0 \rho_s)^{-1}$ , it is natural to expect that it will be dominated by the largest accessible binormal scales  $k_y^0 \rho_s \ll 1$ <sup>1</sup>. At such scales, the system approaches the drift-kinetic limit of gyrokinetics, in which all gyroaverages in (2) are well-approximated by unity operators to leading order. However, in this limit, there is no intrinsic perpendicular scale: the dynamics are scale-invariant [30], and so there is no microscopic mechanism that can be used to determine  $k_y^0$ . The only remaining candidate perpendicular length scales are the sizes  $L_x$  and  $L_y$  of our flux-tube domain in the radial and binormal directions, respectively. However, the flux-tube approximation is predicated on the assumption that the fluctuations remain microscopic in the perpendicular direction (they are ordered  $k_x \sim k_y \sim \rho_s^{-1}$ ). This means that as the perpendicular domain size is increased, there must come a point at which the turbulence, and the resultant heat flux, become independent of it; if this were not the case, then the heat flux would diverge as  $L_x/\rho_s, L_y/\rho_s \rightarrow \infty$ , implying that the local flux-tube approximation is not a valid model of the plasma dynamics. Hence, the heat flux *should* be independent of the perpendicular extent of our flux-tube domain, meaning that the outer scale cannot be set solely by perpendicular considerations; instead, it must be fixed by parallel dynamics. A natural way to determine this scale is through *critical balance*, *viz.*, the condition that the time scales of parallel propagation and perpendicular nonlinear decorrelation be comparable. The logic is straightforward: two points separated along a field line can only remain correlated with one another if information can propagate between them faster than they are decorrelated by the (perpendicular) nonlinearity.<sup>2</sup> This is a standard argument originally developed in the context of MHD turbulence [41–43], where the information is carried by Alfvén waves. In (collisionless) electrostatic gyrokinetic turbulence, the relevant propagation speed is the parallel streaming rate  $\omega_{\parallel} \sim k_{\parallel} v_{\text{th}s}$ , meaning that, at the outer scale, we require, in addition to (9), the balance

$$(t_{\text{nl}}^{-1})^0 \sim \omega_{\parallel}^0 \sim k_{\parallel}^0 v_{\text{th}s} \sim \frac{v_{\text{th}s}}{L_{\parallel}}. \quad (14)$$

Here, and throughout,  $L_{\parallel}$  denotes the characteristic parallel system scale, which may in principle depend on parameters associated with both the plasma equilibrium (*i.e.*, on  $L_{T_s}$ ) and the magnetic equilibrium (*e.g.*, on the safety factor  $q$ ). In the cases that we consider in this paper, we find  $L_{\parallel}$  to be independent of the plasma equilibrium (see the numerical simulations of sections III B, IV B, and V B), but our general approach does not assume such independence. Then,

<sup>1</sup> The fact that the heat flux is dominated by fluctuations at scales  $k_y^0 \rho_s \ll 1$  is not always guaranteed. For example, turbulence driven by the short-wavelength ITG [36–38] will have  $k_y^0 \rho_s \gtrsim 1$  (see, *e.g.*, [39]), wherein (13) would also have to be modified. However, such a state requires the ITG to be stable at larger scales, which is unlikely to be achieved except in the presence of strong equilibrium flow shear (see, *e.g.*, [31]).

<sup>2</sup> Although we here associate  $\omega_{\parallel}$  with the rate of parallel propagation, it may equivalently be interpreted as some characteristic parallel dissipation rate. For instance,  $\omega_{\parallel} \sim k_{\parallel} v_{\text{th}s}$  appearing in (14) represents both the rates of parallel-streaming and (velocity-space) phase mixing associated with Landau damping [40]. In the former case, the critical balance (14) can be interpreted in terms of the causality argument given in the main text; in the latter, the parallel coherence of fluctuations is instead limited (on the small-parallel-scale side) by Landau damping. In either case, however,  $\omega_{\parallel}$  acts to set  $L_{\parallel}$ .

combining (9), (13), and (14), we find the following relationship

$$k_y^o \rho_s \sim \frac{L_{T_s}}{L_{\parallel}}. \quad (15)$$

At first glance, it seems that we have not made any progress, trading the unknown outer-scale binormal wavenumber  $k_y^o \rho_s$  for a similarly unknown parallel system scale  $L_{\parallel}$ . However, the latter is often determined by the magnetic geometry: we will see that, while in a straight magnetic field  $L_{\parallel}$  is the parallel box length (§III), and therefore as artificial as  $L_x$  or  $L_y$ , in axisymmetric toroidal systems, it typically corresponds to the connection length (§IV). It is worth emphasising that, while critical balance is usually discussed in the context of inertial-range dynamics, we are only considering dynamics at the outer scale for the purposes of our emerging theory.

#### F. Heat-flux scaling

Substituting (13) and (15) into (12), we arrive at the following expression for the heat flux:

$$\frac{Q_s}{Q_{\text{gBs}}} \sim \left( \frac{L_{\parallel}}{L_{\text{ref}}} \right) \left( \frac{L_{\text{ref}}}{L_{T_s}} \right)^3 (\mathcal{A}^o)^{-2}, \quad (16)$$

in which  $Q_{\text{gBs}} = n_s T_s v_{\text{th}s} (\rho_s / L_{\text{ref}})^2$  is the gyro-Bohm heat flux and  $L_{\text{ref}}$  is some yet-to-be-specified reference length scale for the plasma equilibrium (e.g., the minor radius  $a$ ). Equation (16) is the most general scaling that can be obtained for the heat flux in electrostatic gyrokinetic turbulence without committing to a particular equilibrium. To make further progress, one must specify the magnetic geometry and equilibrium profiles in order to determine the parallel system scale  $L_{\parallel}$  and outer-scale aspect ratio  $\mathcal{A}^o$ . Note that  $\mathcal{A}^o$  can (and indeed, does) depend on  $L_{\parallel}/L_{\text{ref}}$  and/or  $L_{\text{ref}}/L_{T_s}$ . In the following sections, we examine the predictive power of (16) for slab (§III), axisymmetric (§IV), and non-axisymmetric (§V) geometries.

Before doing so, however, it is worth pausing to review the assumptions that led us here. We began by arguing that in order for there to be an injection of energy into the turbulence in the first place, unstable fluctuations must survive long enough to interact nonlinearly. This motivated the definition of the outer scale (9), determined by the balance between the rates of nonlinear decorrelation (8) and linear growth of the temperature-gradient-driven modes (13). The resulting expression for the heat flux (12) then depended only on the outer-scale binormal wavenumber  $k_y^o \rho_s$  and aspect ratio  $\mathcal{A}^o$ , yet to be determined. However, we could not appeal to any intrinsic perpendicular scale to determine the former owing to the fact that it (generally) lies at large binormal scales, i.e., in the scale-invariant drift-kinetic regime. Instead, we assumed that the dynamic organised themselves so that the rates of parallel propagation and nonlinear decorrelation were comparable at the outer scale, i.e., were in the critical balance (14), leading directly to (16). As promised, this series of steps relied only on simple physical arguments about the competition between the time scales introduced in §IIC. The resulting expression for the electrostatic heat flux (16) should therefore be viewed as the natural and quite general consequence of this competition, rather than the product of detailed or restrictive assumptions.

#### G. Adiabatic responses

As anticipated at the start of this section, we have been considering only the turbulence driven by a single species, either electrons or ions. Such an assumption naturally restricts our consideration to either scales much smaller than the ion Larmor radius,  $k_{\perp} \rho_i \gg 1$ , in the case of ETG-driven turbulence, or scales much larger than it,  $k_{\perp} \rho_i \ll 1$ , in the case of ITG-driven turbulence. In the former limit, ions can be viewed as motionless rings of charge, and their density response  $\delta n_i$  approximately Boltzmann:

$$\frac{\delta n_i}{n_i} = -\frac{Z_i e \delta \phi}{T_i}. \quad (17)$$

The electron density in the large-scale limit does not have quite the same property due to the fact that the parallel streaming of electrons  $\sim k_{\parallel} v_{\text{the}}$  is sufficiently fast on ion time scales that their motion along the equilibrium magnetic field lines allows them effectively to cover the entire flux-surface. As a result, they cannot sustain a density perturbation associated with a flux-surface-averaged (i.e., zonal) potential; any such perturbation is quickly erased by electrons equilibrating the potential over the flux surface. To reflect this, one typically adopts the modified adiabatic electron

response [44–46] when considering ion-scale turbulence, with the zonal component of the potential excused from the Boltzmann response, viz.,

$$\frac{\delta n_e}{n_e} = \frac{e}{T_e} \left( \delta\phi - \langle \delta\phi \rangle_{y,z} \right), \quad (18)$$

where  $\langle \dots \rangle_{y,z}$  denotes the zonal average. Unlike the adiabatic ion response (17), this explicitly privileges zonal perturbations, making them dynamically distinct. We will see that it is precisely this distinction that gives rise to the differences in saturation between ETG- and ITG-driven turbulence, by affecting the outer-scale aspect ratio  $\mathcal{A}^\circ$ .

### III. SLAB GEOMETRY

Let us first consider a homogeneous plasma in a uniform magnetic field oriented along the  $z$  direction, the so-called ‘slab’ geometry. While this case is not of direct relevance to fusion turbulence, it provides the simplest setting in which (16) can be tested, and will allow a reader unfamiliar with these arguments to develop intuition that will prove useful in later sections. The reader more committed to real fusion applications may skip ahead to §IV.

#### A. Slab scalings

With the simplicity of a slab in mind, we focus on electron-scale turbulence driven by an electron-temperature gradient  $L_{T_e}$ , a case that we henceforth refer to as ‘slab ETG’ (sETG). Given that  $L_{T_e}$  is the only non-trivial length scale associated with the plasma equilibrium, we set  $L_{\text{ref}} = L_{T_e}$  in (16). The ion density response is taken to be adiabatic according to (17). Let us take a moment to discuss the implications that this has for the outer-scale aspect ratio  $\mathcal{A}^\circ$ .

The outer scale is, by definition, the scale at which both linear and nonlinear effects are comparable [see (9)]. This balance must then determine the anisotropy of the fluctuations at that scale. Nonlinearly, the evolution of sETG fluctuations is isotropic, so one might expect  $\mathcal{A}^\circ \sim 1$ . This is despite the fact that (linear) energy injection is often associated with so-called ‘streamers’: radially-elongated eddies with a vanishingly small radial wavenumber. A possible resolution is provided by the ‘secondary-instability’ picture of saturation [47–49], which posits that such streamers will go unstable to zonal perturbations that will shear them apart, in so doing generating eddies with  $k_x^\circ \sim k_y^\circ$ . For ITG-driven turbulence, however, such a picture of saturation is less obvious. The modified adiabatic electron response (18) explicitly privileges the role of zonal perturbations since, unlike their non-zonal counterparts, they receive no contribution from the electron dynamics. This makes zonal flows easier to excite [45] and suggests that they could play a more dominant role, potentially breaking the simple  $\mathcal{A}^\circ \sim 1$  expectation. Indeed, we find that simulations of ITG-driven slab turbulence always lie in the Dimits regime [50], suggesting that the presence of curvature-driven ITG is required in order to support strongly driven turbulence (see, e.g., [49, 51]). The adiabatic ion response (17), on the other hand, does not distinguish between zonal and non-zonal perturbations, meaning that, in the absence of any other *a priori* knowledge, it is reasonable to assume that the outer-scale aspect ratio remains order unity,  $\mathcal{A}^\circ \sim 1$ , i.e., that it is independent of both  $L_\parallel$  and  $L_{T_e}$ . It is important to emphasise that  $\mathcal{A}^\circ \sim 1$  does not imply that the turbulence is isotropic at the outer scale, only that whatever outer-scale anisotropy that may exist does not vary with equilibrium quantities. Indeed, we will find that ETG-driven turbulence can have  $\mathcal{A}^\circ$  both smaller and larger than unity while satisfying this scaling.

Our resulting predictions for the heat flux (16), binormal outer scale (15), and aspect ratio are then

$$\frac{Q_e}{Q_{\text{gBe}}} \sim \frac{L_\parallel}{L_{T_e}}, \quad k_y^\circ \rho_e \sim \frac{L_{T_e}}{L_\parallel}, \quad \mathcal{A}^\circ \sim 1, \quad (19)$$

with  $Q_{\text{gBe}} = n_e T_e v_{\text{the}} (\rho_e / L_{T_e})^2$ , recovering the cubic scaling with the electron-temperature gradient anticipated by previous theoretical studies [25, 29, 30]. In (19),  $L_\parallel$  should be interpreted as the parallel extent of the simulation domain, since in slab geometry there is no other intrinsic parallel length in the absence of finite magnetic shear. Equivalently, the longest distance a turbulent eddy can extend along the field line is the box length itself and so this must set the parallel system scale. Hence,  $L_\parallel / L_{T_e}$  becomes the sole physical input parameter to the system.

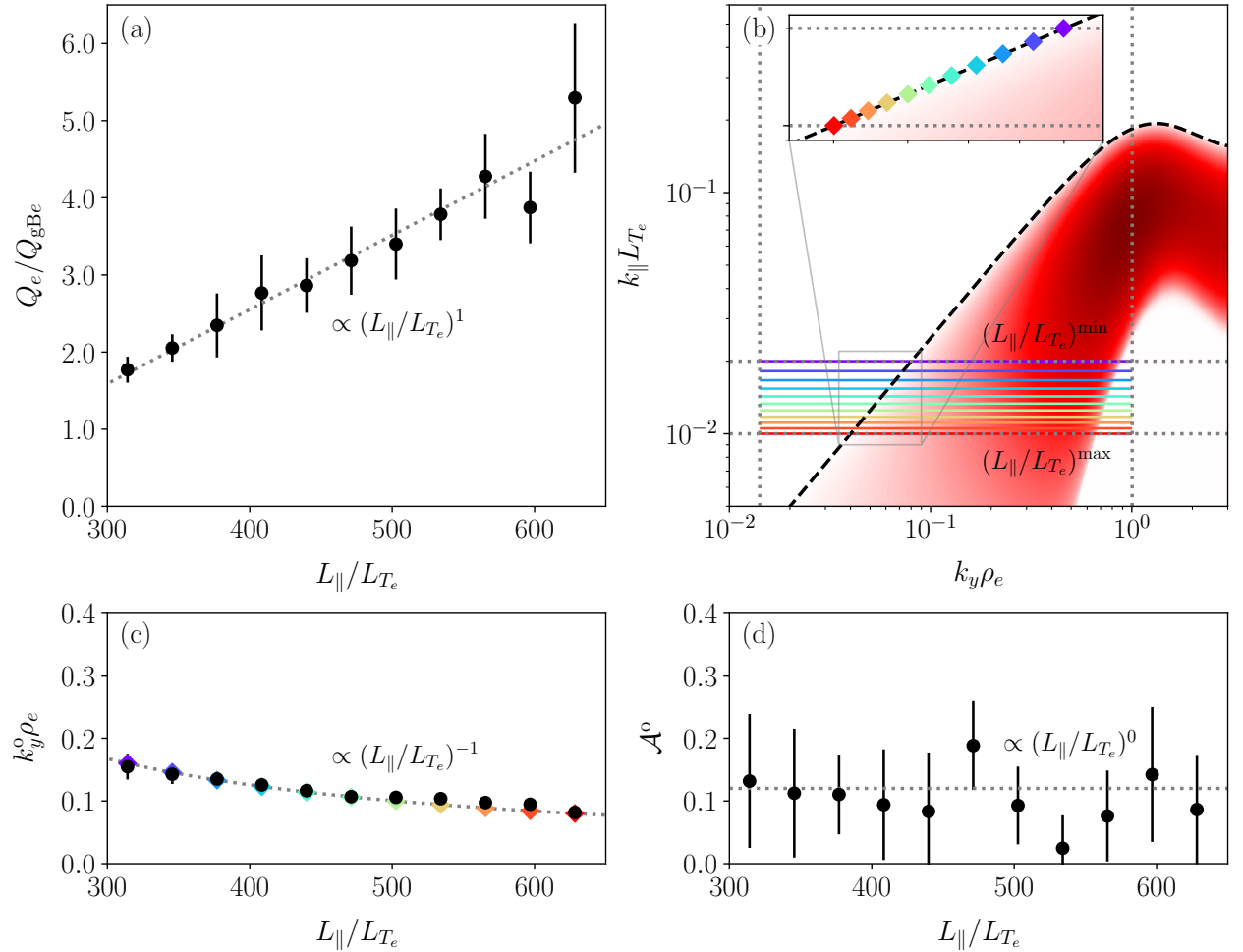


FIG. 1. Scaling results from the sETG simulations. (a) Time-averaged gyro-Bohm-normalised heat flux  $Q_e/Q_{gBe}$  [here  $Q_{gBe} = n_e T_e v_{the} (\rho_e/L_{T_e})^2$ ] as a function of  $L_{||}/L_{T_e}$  (black circles), with the error bars showing the standard deviation over time. The dotted line shows the expected scaling [first expression in (19)]. (b) Contour plot of the unstable solutions sETG dispersion relation (20) in the  $(k_y, k_{||})$  plane for  $k_x = 0$ ,  $Z_i = 1$ , and  $T_i = T_e$ , with the dashed line showing the associated stability boundary (21). The vertical dotted lines indicate to the minimum and maximum  $k_y \rho_e$  in the simulation domain, with the horizontal dotted lines bounding the range of parallel wavenumbers corresponding to the different values of  $L_{||}/L_{T_e}$  in panel (a), each indicated by one of the horizontal coloured lines. The coloured diamonds in the inset denote the location of the intersection of these lines with the stability boundary. The maximum value of  $k_{||} L_{T_e} = 0.6$  for all simulations corresponds to the top edge of the plot. (c) Time-averaged value of the binormal outer scale  $k_y^o \rho_e$  (black circles), with the error bars showing the standard deviation over time. The coloured diamonds are values of  $k_y \rho_s$  from those in panel (b) multiplied by an order-unity constant [see the discussion following (22)]. The dotted line shows the expected scaling [the second expression in (19)]. (d) Time-averaged outer-scale aspect ratio  $A^o$  (black circles), with the error bars showing the standard deviation over time. The dotted line shows the expected scaling [the third expression in (19)].

## B. sETG simulations

To test the predictions (19), we solve the electrostatic gyrokinetic system of equations (2) and (3) in slab geometry using GX [7], the code employed for all simulations in this paper. The homogeneous nature of the magnetic field allows periodic boundary conditions along  $z$  to be used. We vary  $L_{||}/L_{T_e}$  by a factor of two, increasing the parallel resolution accordingly to maintain the same maximum parallel wavenumber  $k_{||} L_{T_e}$  in the box. We did not perform simulations at  $L_{||}/L_{T_e} < 300$  as these would not be sufficiently strongly driven to realise the scalings (19). The perpendicular box sizes and corresponding resolution are held constant. Further details about the numerical setup can be found in §A (see the row labelled ‘sETG’ in table I).

The results of this scan are shown in figure 1. In panel (a), we plot the turbulent electron heat flux  $Q_e/Q_{gBe}$  averaged over the last 80% of each simulation’s running time [see figure 2(a)], with the error bars showing the standard deviation

over the same period. The first prediction of (19) — that the gyroBohm-normalised heat flux should scale linearly with  $L_{\parallel}/L_{T_e}$  — is clearly borne out by the data. At larger  $L_{\parallel}/L_{T_e}$ , the error bars become noticeably larger, reflecting the presence of stronger oscillations on longer time scales in the heat flux [see figure 2(a)]. Rather than being coincidental, this is a direct consequence of the underlying scale invariance of drift kinetics (see [30]).

To see why this scaling of the heat flux is, in a sense, inevitable in this simple slab case, it will be instructive to examine the linear dispersion relation for slab ETG modes [12, 13]:

$$1 + \frac{T_e}{Z_i T_i} + \left\{ \zeta Z - \zeta_* \left[ \zeta + \left( \zeta^2 - \frac{1}{2} \right) Z \right] \right\} \Gamma_0 + \zeta_* b_e \Gamma_1 Z = 0, \quad (20)$$

where  $\zeta = \omega/|k_{\parallel}|v_{\text{the}}$  and  $\zeta_* = \eta_e \omega_{*e}/|k_{\parallel}|v_{\text{the}}$  are the normalised frequencies,  $Z = Z(\zeta)$  is the standard plasma dispersion function [52, 53],  $\Gamma_0(b_e) = I_0(b_e)e^{-b_e}$ ,  $\Gamma_1(b_e) = [I_0(b_e) - I_1(b_e)]e^{-b_e}$ , with  $b_e = k_{\perp}^2 \rho_e^2/2$ , and  $I_0, I_1$  are the modified Bessel functions of the first kind [54]. The associated stability boundary — the parallel wavenumber above which solutions are no longer unstable — is

$$|k_{\parallel}|L_{T_e} = \frac{k_y \rho_e}{2} \left[ \frac{(\Gamma_0/2 + b_e \Gamma_1) \Gamma_0}{(1 + T_e/Z_i T_i)(1 + T_e/Z_i T_i - \Gamma_0)} \right]^{1/2}. \quad (21)$$

This is plotted in the  $(k_y, k_{\parallel})$  plane for  $k_x = 0$  in figure 1(b), alongside the unstable solutions to (20).

Now consider a simulation with a given value of  $L_{\parallel}/L_{T_e}$ , with which we can associate a minimum parallel wavenumber  $k_{\parallel}^{\min} = 2\pi/L_{\parallel}$  accessible by the fluctuations (set by the parallel box size). As we argued at the beginning of §II E, there is no intrinsic perpendicular scale at  $k_{\perp} \rho_e \ll 1$  to set  $k_y^o$ . Consequently, at any given  $k_{\parallel}$ , the potential location of the outer scale is pushed to the largest binormal scale that remains unstable; equivalently,  $k_y^o \rho_e$  must lie on, or close to, the linear stability boundary (21). Then, according to the critical-balance arguments of §II E, the finite parallel extent of the domain pins the outer scale to the intersection of the stability boundary and the line  $k_{\parallel} = k_{\parallel}^{\min}$  [viz., the solutions to (21) with  $k_{\parallel} = k_{\parallel}^{\min}$ ], which are marked by coloured diamonds in figure 1(b), (c). It follows that the outer scale observed in nonlinear simulations should coincide with the coloured diamonds along the stability boundary plotted in the inset of panel (b). Panel (c) shows that this expectation is correct: the measured outer-scale wavenumbers, defined as those that maximise the binormal heat-flux spectrum [for  $s = e$ ; see (10)]

$$Q_s(k_y) = \sum_{k_x} \langle Q_{s\mathbf{k}_{\perp}}(k_x, k_y, z) \rangle_z, \quad (22)$$

closely track both theoretical prediction of (19) and the values obtained directly from the linear stability boundary, so much so in the latter case that the latter almost completely overlap with the measured values. Note that we have multiplied the latter values by an order-unity constant (in this case, a factor of two) to obtain this level of agreement; the scaling estimate for the binormal outer scale [the second expression in (19)] omits such numerical factors. Plotting the binormal spectrum itself in figure 2(b), it is obvious that the peak moves towards larger scales as  $L_{\parallel}/L_{T_e}$  is increased. This provides further confirmation of the validity of the simple physical arguments underpinning the results of §II.

Finally, to examine the scaling of the outer-scale aspect ratio  $\mathcal{A}^o$ , we need to measure the outer-scale radial wavenumber  $k_x^o \rho_e$ . This is less straightforward than for the binormal outer scale, owing to the fact that the radial spectrum of the heat flux [for  $s = e$ ; see (10)]

$$Q_s(k_x) = \sum_{k_y} \langle Q_{s\mathbf{k}_{\perp}}(k_x, k_y, z) \rangle_z, \quad (23)$$

is typically observed to peak at  $k_x = 0$  in fusion-relevant studies of gyrokinetic turbulence, with the present case being no exception [see figure 2(c)]. Instead, we exploit the fact that in such cases the radial spectrum generally exhibits a spectral break at some finite value of  $k_x$ : at scales larger than the break, the slope of the spectrum is either shallow or flat, while at scales smaller than it, it exhibits some slope characteristic of inertial-range dynamics. We identify the wavenumber location of this break to be the radial outer scale  $k_x^o \rho_e$ , which we extract by fitting a broken power-law to the measured spectrum. This is done by fitting to the spectrum, at each instant in time, two power-law segments separated by a single break point. For each candidate break location, we measure the combined error from fitting the power laws on either side and select the break location that minimises this error, i.e., the best broken-power-law fit to the spectrum.

This choice of radial outer scale can be motivated as follows. As we discussed following (11), our scaling estimate for the heat flux assumes that  $\delta\phi_{k_y}$  decays sufficiently quickly as a function of the binormal wavenumber. Given that

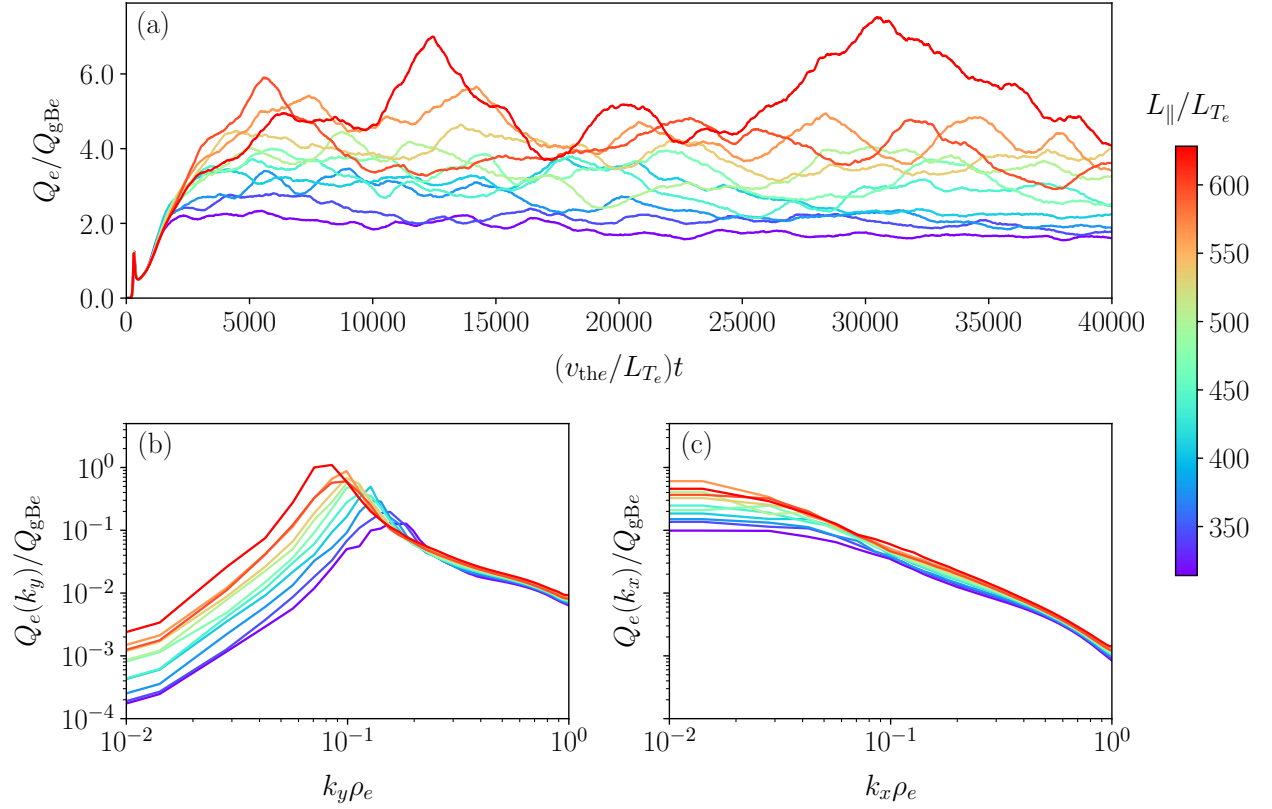


FIG. 2. Gyro-Bohm-normalised heat-flux time traces and spectra from the sETG simulations, with the colours indicating the value of  $L_{\parallel}/L_{T_e}$  for a given simulation: (a) heat flux as a function of time; (b) time-averaged binormal spectrum of the heat flux (22); (c) time-averaged radial spectrum of the heat flux (23).

we expect the turbulence to be roughly isotropic in the inertial range (see [24, 25, 30] and appendix A of [31]), the fluctuations therein will also decay as a function of  $k_x$ . This means that the break in the spectrum must correspond to the large-scale end of the inertial range, and thus the outer scale, by definition. Note that we have deliberately not attempted to offer a dynamical explanation for the flat spectrum on scales  $k_x < k_x^o$  because the details thereof are irrelevant for our scaling predictions (and will in all likelihood depend on specifics of the underlying equilibrium in a non-universal way). Indeed, this behaviour of the spectrum could come across as surprising for readers more familiar with studies of isotropic plasma turbulence. For a homogeneous 2D isotropic field, the low- $k_{\perp}$  spectrum can be shown to scale as  $k_{\perp}^3$  (see, e.g., appendix A of [40]), though a  $k_{\perp}^1$  scaling is also possible in some contexts [55]. Either of these scalings initially appear inconsistent with the flat or very shallow  $k_x$  spectrum at large scales seen here. A possible resolution is that the turbulence above the outer scale is manifestly *not* isotropic, with more power contained in binormal fluctuations [compare the large-scale behaviour of the spectra in panels (b) and (c) of figure 2], and so we would not necessarily expect these kinematic scalings to hold in the present context.

Applying the procedure outlined above, we find that the resulting outer-scale aspect ratio  $\mathcal{A}^o = k_x^o/k_y^o$  is approximately constant over the full range of  $L_{\parallel}/L_{T_e}$  [see figure 1(d)], in agreement with the third prediction of (19). This supports our earlier claim that the adiabatic ion response (17) does not promote any scaling of  $\mathcal{A}^o$  with equilibrium parameters. We will find that this is also the case for ETG-driven turbulence in the axisymmetric geometry considered in the next section, whereas ITG-driven turbulence displays markedly different behaviour. It is worth noting that the measured value of  $\mathcal{A}^o$  is numerically small [ $\mathcal{A}^o \approx 0.1$  in figure 1(d)], which can have important consequences in the presence of externally imposed flow shear: recent theoretical work [31] has shown that eddies with  $\mathcal{A}^o \ll 1$  are suppressed more effectively by the shear than those with  $\mathcal{A}^o \gtrsim 1$ .

#### IV. AXISYMMETRIC GEOMETRY

Let us now consider the predictions presented in §II in the context of axisymmetric toroidal geometry, treating both ETG- and ITG-driven turbulence. We take  $\psi$  to be the poloidal magnetic flux divided by  $2\pi$  and define the field-line

label as  $\alpha = \zeta - q(\psi)\theta$ , where  $\zeta$  is the toroidal angle (the symmetry angle of the axisymmetric equilibrium),  $\theta$  is the straight-field-line poloidal angle, and  $q$  is the safety factor [56, 57]. The parallel coordinate is chosen as  $z = \theta$ , with  $z = 0$  at the outboard midplane of the device.

### A. Tokamak scalings

As in the slab case, our task is to determine both the parallel system scale  $L_{\parallel}$  and outer-scale aspect ratio  $\mathcal{A}^o$ , since together they set the heat-flux scaling (16). Following previous studies [24–26, 30], we conjecture that the former is set by the distance along the mean field from the outboard to inboard sides of the device, i.e., the connection length  $\sim qR$ , with  $R$  the major radius. The reasoning for this is straightforward: electrostatic temperature-gradient driven instabilities like curvature-driven ETG and ITG are localised in the regions of ‘bad’ (destabilising) curvature, typically peaked at the outboard midplane, and are stabilised once they extend into the regions of ‘good’ (stabilising) curvature. To within factors of order unity, this distance is the connection length. We note that this is not a unique possibility, and indeed may fail for highly-shaped plasmas: e.g., [58, 59] found that, while curvature-driven ETG remained localised to the good-curvature regions in the pedestal, slab ETG modes were simultaneously active at higher values of the poloidal angle. Nevertheless,  $L_{\parallel} \sim qR$  represents the best *a priori* guess for core-relevant turbulence and is, as we will see, supported by our simulations. Since, ETG and ITG have isomorphic collisionless linear dispersion relations<sup>3</sup>, we estimate  $L_{\parallel} \sim qR$  in both cases.

It follows that any difference between the heat-flux scaling in ETG- and ITG-driven turbulence must originate from the aspect ratio  $\mathcal{A}^o$ . Motivated by the results of the previous section, we expect the aspect ratio in ETG once again to be independent of both  $L_{\parallel}$  and  $L_{T_e}$ , viz.,  $\mathcal{A}^o \sim 1$ <sup>4</sup>. Substituting this into (16) and using our expression for the parallel system scale  $L_{\parallel} \sim qR$ , we obtain the following predictions for saturated ETG turbulence in axisymmetric geometry:

$$\frac{Q_e}{Q_{\text{gBe}}} \sim q \left( \frac{R}{a} \right) \left( \frac{a}{L_{T_e}} \right)^3, \quad k_y^o \rho_e \sim \frac{L_{T_e}}{qR}, \quad \mathcal{A}^o \sim 1. \quad (24)$$

Note that these results are in fact identical to those in the sETG case (19), except we have now specified a specific form for the parallel system scale and set our reference length scale  $L_{\text{ref}}$  to be the minor radius  $a$ , so there is no  $L_{T_e}$  dependence hiding in the definition of  $Q_{\text{gBe}}$ .

For ITG turbulence, however, the situation is different. As discussed in §II G, the modified adiabatic electron response (18) explicitly privileges zonal flows by making them easier to drive than the  $k_y \neq 0$  modes [45]. Naturally, we might expect zonal fluctuations to play a key role in determining the outer scale. Indeed, recent work [26, 62] has shown that this gives rise to a novel zonal mode — the so-called ‘toroidal secondary’ — that grows and propagates due to the combined effects of zonal-flow shearing, advection by the radial component of the magnetic drifts, and compressibility of zonal flows in toroidal geometry. Above a certain threshold in the amplitudes, small-scale toroidal secondary modes become unstable and shear apart what would otherwise be large-scale turbulent eddies, forcing the turbulence to remain close to this threshold. The threshold itself is set by a balance between the ITG growth rate at the outer scale and the time scale associated with the radial magnetic drifts, viz.,

$$\gamma_{k_y^o} \sim \omega_{\text{di},x}^o \sim \frac{k_x^o \rho_i v_{\text{thi}}}{2R} \quad \Rightarrow \quad \mathcal{A}^o \sim \frac{R}{L_{T_i}}, \quad (25)$$

where we have used (13). The combination of (9), (14), and (25) is referred to in the literature as ‘grand critical balance’, and is supported by experimental measurements of ion-scale fluctuations in MAST [27]. In the present context, the effect of the toroidal secondary mode can therefore be interpreted as setting the outer-scale aspect ratio of ITG turbulence: as the temperature gradient increases, the aspect ratio of the eddies must also increase, driving the system to smaller radial scales in order to avoid becoming unstable to the toroidal secondary mode. Substituting (25) into (16) and once again using our expression for the parallel system scale  $L_{\parallel} \sim qR$ , our resulting set of predictions

<sup>3</sup> Consider the linearised gyrokinetic equation (2) for a given mode with  $k_y \neq 0$ . When written in terms of an appropriately normalised potential  $\varphi = Z_s e \delta \phi / T_s$ , this is identical for electrons ( $s = e$ ) and ions ( $s = i$ ). Doing the same for quasineutrality (3), it is straightforward to see that the resultant linear systems of equations are also identical up to the replacement  $T_e / Z_i T_i \mapsto (T_e / Z_i T_i)^{-1}$ , converting the ITG case into the ETG one.

<sup>4</sup> This is not the only possible outcome. Previous studies (see, e.g., [60, 61]) have shown that ETG turbulence can, in some cases, be regulated at long times by strong zonal flows that grow slowly and eventually dominate the saturation process. In our simulations, however, we see no evidence of such long-time growth (possibly due to the strong drive), and so we regard  $\mathcal{A}^o \sim 1$  as the most straightforward *a priori* estimate.

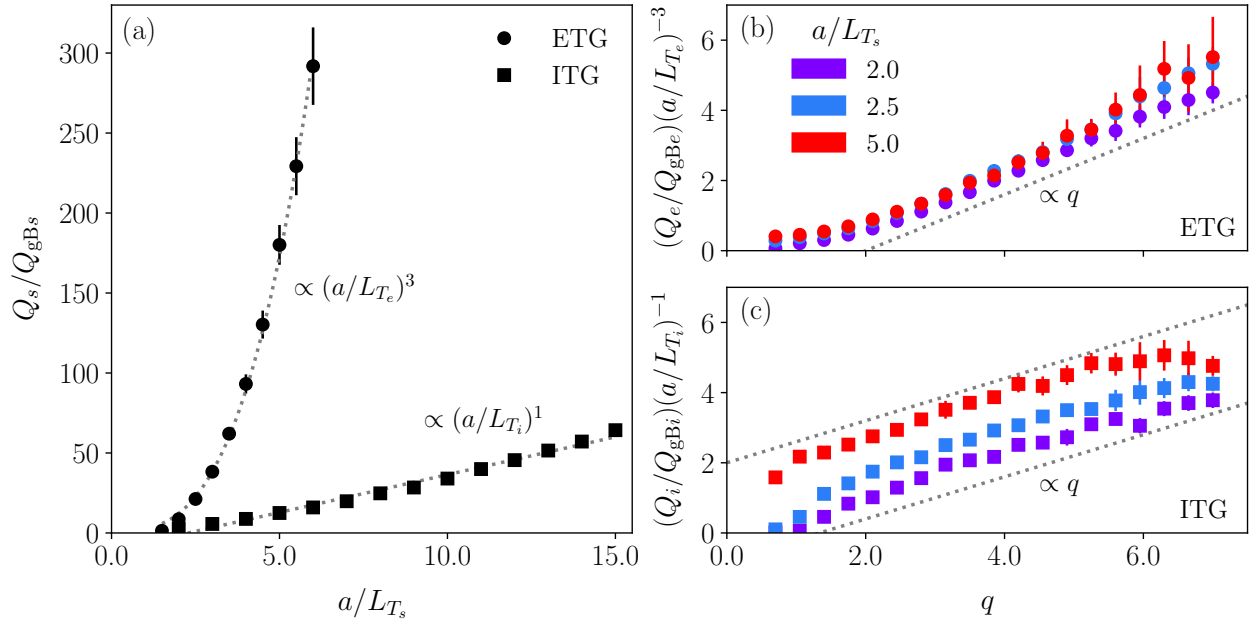


FIG. 3. Heat-flux scalings from the CBC simulations. In all panels, the circles correspond to ETG cases and squares to ITG ones. The error bars show the standard deviation over time. (a) Heat flux as a function of the normalised temperature gradient  $a/L_{T_s}$ , with the dotted lines showing the predicted scalings [first expressions in (24) and (26)]. (b) Electron heat flux rescaled by  $(a/L_{T_e})^{-3}$  for three different values of the normalised temperature gradient, indicated by the different colours. The dotted line shows the predicted scaling [first expressions in (24) and (26)]. (c) The same as in (b) except the ion heat flux is rescaled by  $(a/L_{T_i})^{-1}$ .

for saturated ITG turbulence are:

$$\frac{Q_i}{Q_{gBi}} \sim q \left( \frac{a}{R} \right) \left( \frac{a}{L_{T_i}} \right), \quad k_y^o \rho_i \sim \frac{L_{T_i}}{qR}, \quad \mathcal{A}^o \sim \frac{R}{L_{T_i}}. \quad (26)$$

These latter estimates are different to those originally proposed for ITG turbulence by [24], who were unaware of the toroidal secondary mode.

Comparing (24) and (26), it is clear that ETG is predicted to exhibit a much stiffer scaling with the temperature gradient than for ITG, a direct consequence of the difference in how the outer-scale aspect ratio is set. This comparison highlights a fundamental asymmetry between ETG- and ITG-driven turbulence in toroidal systems: although they share the same parallel connection length, it is the distinct role of zonal dynamics (or lack thereof) that controls the outer-scale anisotropy and ultimately the scaling of the heat flux. We note that while this asymmetry is also responsible for the emergence of the Dimits regime [47, 49–51, 63–68] in the ITG-driven case, we do not consider such dynamics here due to the assumption of strong linear drive meaning, by definition, that we are sufficiently far from any characteristic linear or nonlinear critical gradients.

## B. CBC simulations

To put the above predictions on a quantitative basis, we perform simulations of both ETG- and ITG-driven turbulence in the well-studied ‘Cyclone-base-case’ (CBC) geometry [50, 69], in which flux surfaces have a circular cross section with aspect ratio  $R/a = 2.78$ . We consider dynamics on the flux surface located at mid-radius  $r/a = 0.5$ , with the normalized magnetic shear  $\hat{s} = 0.2$ <sup>5</sup>. The simulations evolve a single kinetic species, either electrons or ions, employing the appropriate adiabatic closure, viz. (17) for adiabatic ions or (18) for adiabatic electrons. The normalized density gradient is fixed at  $a/L_{n_s} = 0.8$  throughout, while both the normalized temperature gradient

<sup>5</sup> This magnetic shear is lower than the more standard  $\hat{s} = 0.8$  usually employed in CBC studies at  $r/a = 0.5$ . We adopt this reduced value to avoid the well-documented issue of the ETG instability’s failure to saturate at higher shear (see, e.g., [14, 15]). Since our focus is on the mechanism of ETG saturation when it occurs, rather than on the conditions under which saturation may fail, we leave the latter question aside for the present study.

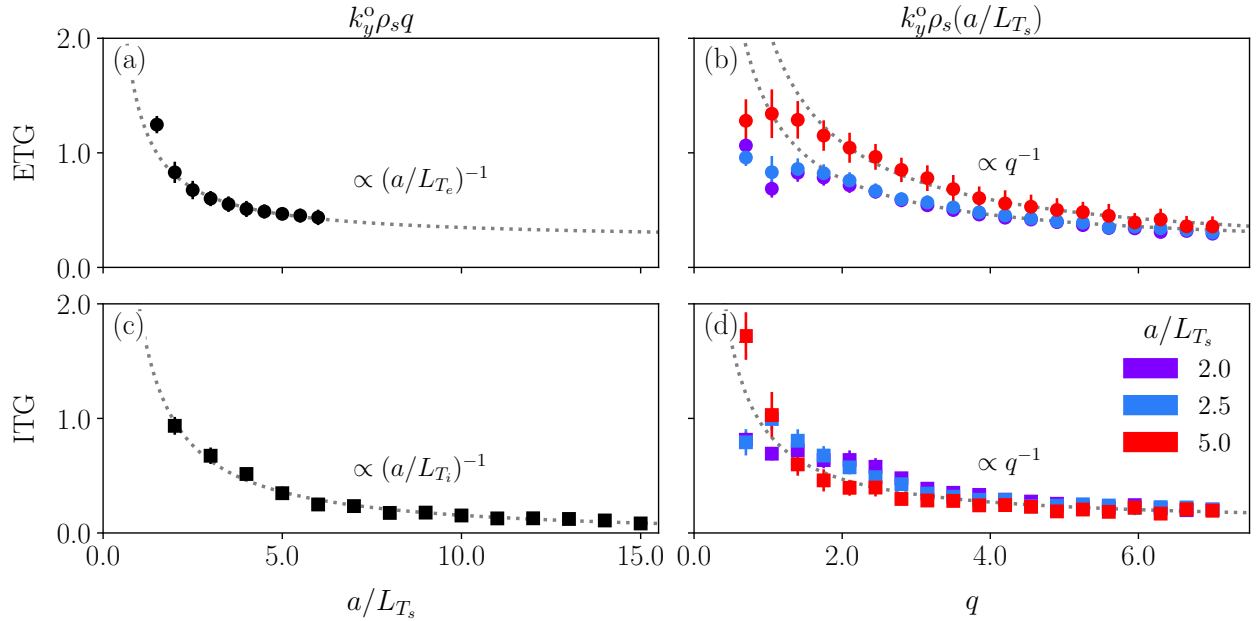


FIG. 4. Outer-scale binormal wavenumber scalings from the same CBC simulations as in figure 3. In all panels, the time-averaged values of  $k_y^o \rho_s$  are indicated by the points, with circles corresponding to ETG cases and squares to ITG ones. The error bars show the standard deviation over time, while the dotted lines show the predicted scalings [second expressions in (24) and (26)] at large  $a/L_{T_s}$ . (a) and (c):  $k_y^o \rho_s$  rescaled by the safety factor  $q$  as a function of the normalised temperature gradient  $a/L_{T_s}$  for ETG and ITG, respectively. (b) and (d):  $k_y^o \rho_s$  rescaled by  $a/L_{T_s}$  as a function of  $q$  at three different values of  $a/L_{T_s}$ , indicated by the different colours, for ETG and ITG, respectively.

$a/L_{T_s}$  and safety factor  $q$  are allowed to vary. The parallel simulation domain is extended for a single poloidal turn, viz.,  $\theta \in [-\pi, \pi]$ . Unless otherwise stated, all data has been time-averaged over the last 80% of the simulation time (see figures 13, 14, and 15 in §B), with any error bars showing the standard deviation over the same time period. Further details about the numerical setup can be found in §A.

Let us first focus on the predictions for the scaling of the heat fluxes, i.e., the first expressions in (24) and (26). Figure 3(a) shows the time-averaged gyro-Bohm-normalised heat fluxes from scans in  $a/L_{T_s}$  for each species (labelled ‘CBC ETG  $L_{T_e}$ ’ and ‘CBC ITG  $L_{T_i}$ ’ in table I). The data displays a striking agreement with the predicted cubic and linear scalings for ETG and ITG, respectively. The ETG simulations could not be extended to higher values of  $a/L_{T_e}$  than those shown due to the computational constraints imposed by the saturated large-amplitude fluctuations ( $\sim 10^3$  in normalised units) at these values. Panels (b) and (c) show the dependence of the heat fluxes as functions of the safety factor  $q$  for three different values of the normalised temperature gradient  $a/L_{T_s}$ , with the data rescaled by the predicted temperature-gradient scalings (cubic for ETG, linear for ITG). In both cases, the expected linear dependence on  $q$  — here acting as a proxy for the parallel system scale  $L_{\parallel} \sim qR$  — is clearly reproduced. These panels also reinforce the temperature-gradient scaling: once rescaled, the datasets from the  $q$ -scans at different  $a/L_{T_s}$  collapse to within order-unity of each other, despite the underlying heat fluxes varying by more than an order of magnitude. The data collapse is somewhat less precise for ITG, which is not unexpected, since the chosen temperature gradients correspond to turbulence that is less strongly driven than in the ETG case (due to the presence of the Dimits shift in the former).

Having established that the heat fluxes follow the predicted scalings with both  $a/L_{T_s}$  and  $q$ , we now turn to the outer-scale binormal wavenumber  $k_y^o \rho_s$  and the aspect ratio  $\mathcal{A}^o$ , whose behaviour provides a more detailed test of the asymptotic scaling arguments underlying these results. We measure these in the same way as in §III, viz.,  $k_y^o \rho_s$  is taken to be the wavenumber that maximises the binormal spectrum of the heat flux, while the  $k_x^o \rho_s$  that enters into  $\mathcal{A}^o$  is identified with the spectral break in the radial heat-flux spectrum. Figure 4 shows the values of  $k_y^o \rho_s$  from the same set of simulations as the heat fluxes in figure 3. Panels (a) and (c) are plots of  $k_y^o \rho_s$  as a function of the normalised temperature gradients  $a/L_{T_s}$ , with the results following closely the predicted  $(a/L_{T_s})^{-1}$  scaling from the second expressions in (24) and (26). Panels (b) and (d) show  $k_y^o \rho_s$  rescaled by  $a/L_{T_s}$ , now plotted against the safety factor  $q$  for three different values of the temperature gradient. Here too the data reproduces the predicted  $q^{-1}$  dependence, with the departures at lower values of  $q$  likely reflecting the approach to marginal stability, a regime where our asymptotic predictions are not expected to hold. The corresponding outer-scale aspect ratios  $\mathcal{A}^o$  are shown

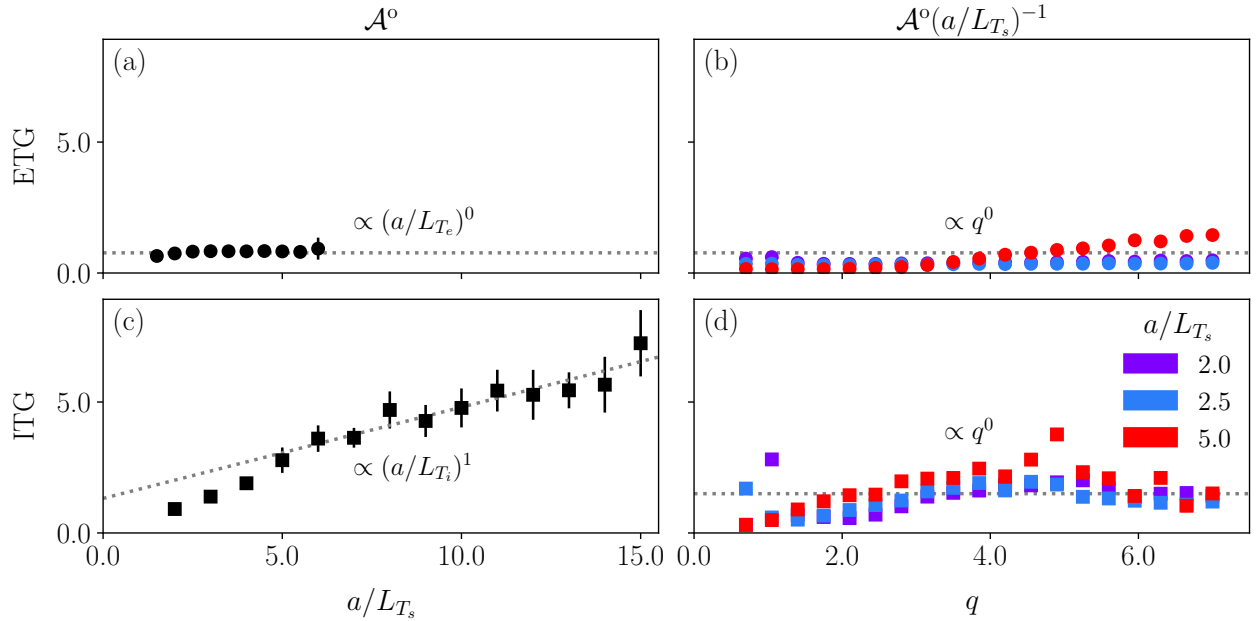


FIG. 5. Outer-scale aspect ratio scalings from the same CBC simulations as in figure 3. In all panels, the time-averaged values of  $\mathcal{A}^o$  are indicated by the points, with circles corresponding to ETG cases and squares to ITG ones. The error bars show the standard deviation over time, while the dotted lines show the predicted scalings [third expressions in (24) and (26)]. (a) and (c):  $\mathcal{A}^o$  as a function of the normalised temperature gradient  $a/L_{T_s}$  for ETG and ITG, respectively. (b) and (d):  $\mathcal{A}^o$  rescaled by  $a/L_{T_s}$  as a function of  $q$  at three different values of  $a/L_{T_s}$ , indicated by the different colours, for ETG and ITG, respectively.

in figure 5. Panels (a) and (c) are plots of  $\mathcal{A}^o$  as a function of  $a/L_{T_s}$ . In the ETG case,  $\mathcal{A}^o$  remains essentially constant, whereas in the ITG case, it varies by nearly an order of magnitude. Thus, both ETG and ITG are consistent with their respective  $(a/L_{T_e})^0$  and  $(a/L_{T_i})^1$  predictions [the third expressions in (24) and (26)]. Panels (b) and (d) show  $\mathcal{A}^o$  from  $q$ -scans at fixed  $a/L_{T_s}$ , confirming the predicted independence on  $q$ : despite the latter varying by an order of magnitude, the aspect ratios change only by factors of order unity [cf. figure 1(d)]. To illustrate more vividly this contrast in behaviour between ETG and ITG, in figure 6 we plot snapshots of the perturbed electrostatic potential  $\delta\phi$  in CBC simulations with  $a/L_{T_s} = 5.0$  and  $q = 2.0$  during both the linear and saturated phases of the turbulent evolution. The linear phase [panels (a) and (c)] looks almost identical for both ETG and ITG; this is to be expected given that their linear dispersion relations are isomorphic, and both simulation domains are the same when measured in units of the relevant gyroradius. The saturated phases, however, are manifestly distinct [panels (b) and (d)]. The ETG turbulence exhibits a preference for radially-elongated structures ( $\mathcal{A}^o \approx 0.8$ ), while its ITG counterpart displays very fine-scale structure in the radial direction ( $\mathcal{A}^o \approx 2.8$ ), consistent with it being limited by the toroidal secondary mode [26, 62].

The stark visual contrast seen in figure 6 highlights the fundamentally different ways in which ETG and ITG turbulence are regulated in axisymmetric toroidal geometry. Taken together, these results demonstrate that the heat flux, binormal outer scale, and aspect ratio behave precisely as anticipated in (24) and (26): ETG turbulence retains a roughly constant outer-scale aspect ratio as a function of equilibrium parameters, viz.,  $\mathcal{A}^o \sim 1$ , while ITG turbulence is strongly shaped by zonal-flow dynamics, leading to systematically larger aspect ratios as the drive increases,  $\mathcal{A}^o \sim R/L_{T_i}$ . These differences translate directly into the heat-flux scalings: ETG turbulence exhibits a cubic dependence on the normalised temperature gradient, while ITG turbulence is constrained to scale only linearly. Readers concerned that these results are specific to the CBC geometry used here may be reassured by the fact that such behaviour has, at least for ETG, been observed in other contexts: e.g., [70] found a cubic scaling with the temperature gradient in their investigations of nonlinear pedestal turbulence driven by ETG modes [see their equation (1), and the following discussion] — but of course it will be valuable to build a body of evidence based on many other configurations, standard or otherwise.

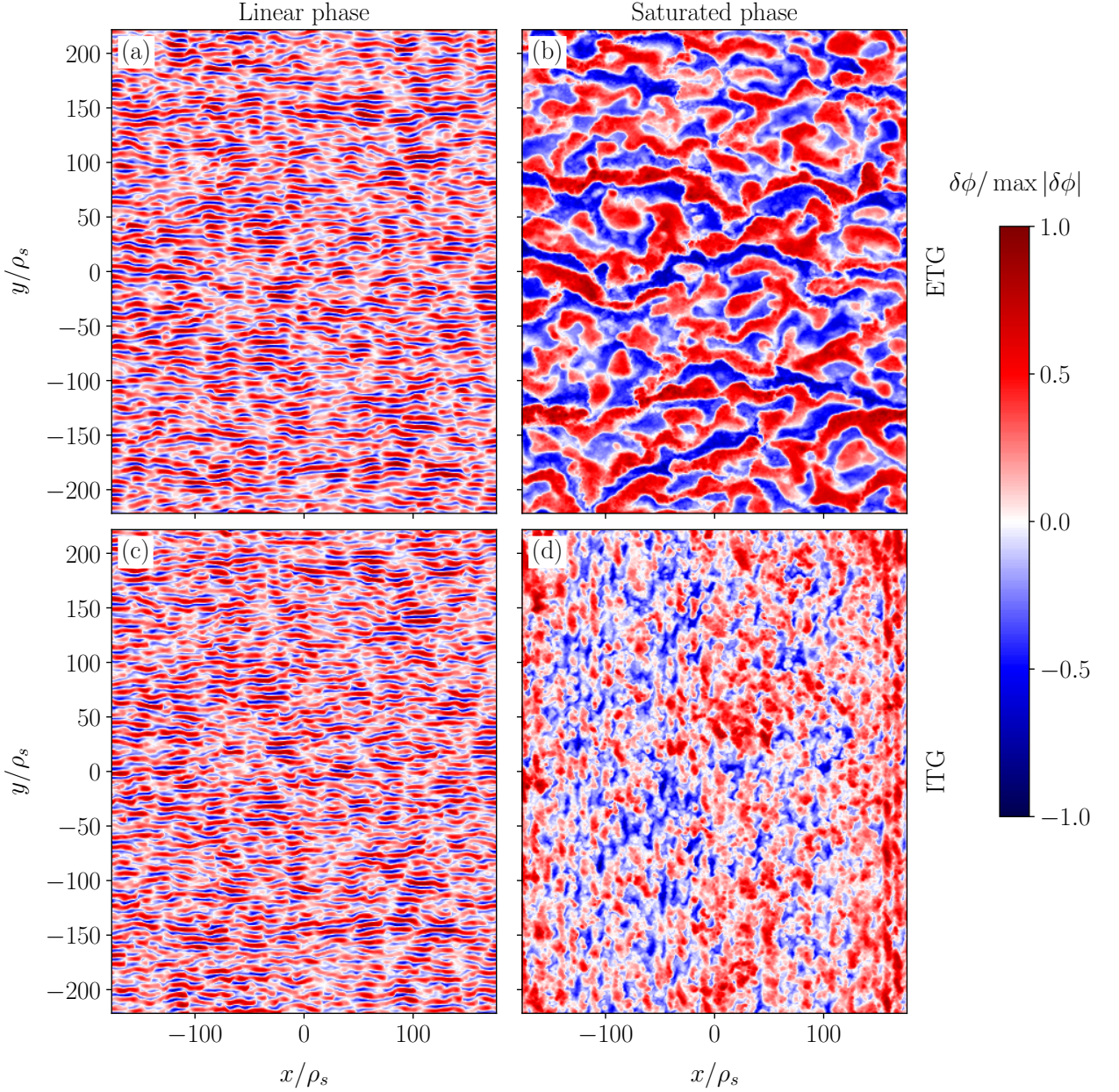


FIG. 6. Snapshots of the perturbed electrostatic potential  $\delta\phi$  at  $\theta = 0$  normalised to its instantaneous maximum value from CBC simulations with  $a/L_{T_s} = 5.0$  and  $q = 2.0$ . The left and right columns show the (nonlinear) simulations during the linear and saturated phases, respectively; the top and bottom rows correspond to ETG and ITG turbulence, respectively. All panels show the entire simulation domain with the appropriate aspect ratio. The difference in the saturated states, and their associated outer-scale aspect ratios, is evident despite the almost identical linear phase.

## V. NON-AXISYMMETRIC GEOMETRY

Continuing the theme of increasing geometrical complexity, we now consider the predictions of §II in the context of fully three-dimensional toroidal (i.e., stellarator) geometry, once again treating both ETG- and ITG-driven turbulence. We take  $\psi$  to be the toroidal magnetic flux divided by  $2\pi$  and define the field-line label as  $\alpha = \theta - \iota\zeta$ , in which  $\zeta$  and  $\theta$  are the straight-field-line toroidal and poloidal angles, respectively, and  $\iota = 1/q$  is the rotational transform. As previously, we adopt  $z = \theta$  as the parallel coordinate. The key questions remain how both the parallel system scale  $L_{\parallel}$  and the outer-scale anisotropy  $\mathcal{A}^o$  are determined in this geometry.

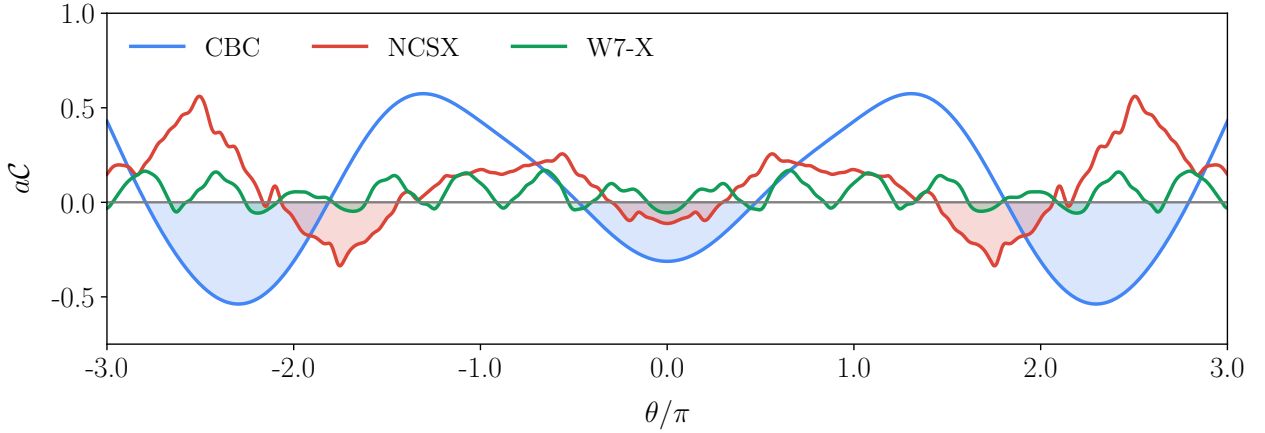


FIG. 7. Local magnetic curvature (27) as a function of the parallel coordinate  $z = \theta$  for the  $\alpha = 0$  flux tube centred at  $\theta = \zeta = 0$  and  $r/a = \sqrt{\psi/\psi_{LCFS}} = 0.5$ , and normalised to the minor radius  $a$ . The colours indicate different magnetic equilibria, while the shaded regions correspond to the regions of bad curvature.

### A. Stellarator scalings

Determining  $L_{\parallel}$  in stellarator geometry is considerably more challenging than in the axisymmetric case. In the latter, we argued that  $L_{\parallel}$  was set by the connection length  $\sim qR$  because it was an effective measure of the distance between good- and bad-curvature regions in a tokamak. However, such a simple picture does not obviously carry over to stellarators, where regions of good and bad curvature are distributed along the field lines in a far more complicated way. To illustrate this, consider the local magnetic curvature for electrostatic modes with  $k_x = 0$  (cf. equation (2.30) of [33]):

$$\mathcal{C}(z) = \frac{B_0}{B} (\mathbf{b} \times \nabla \log B) \cdot \nabla y. \quad (27)$$

Defined in this way,  $\mathcal{C} > 0$  and  $\mathcal{C} < 0$  correspond to regions of good and bad curvature, meaning that we expect electrostatic modes to be unstable where  $\mathcal{C} < 0$  [33, 71]. In figure 7, we plot (27) for the  $\alpha = 0$  field line centred at  $\theta = \zeta = 0$  in three different magnetic equilibria: the CBC geometry considered in §IVB, the National Compact Stellarator Experiment (NCSX, [72]), and the high-mirror configuration of Wendelstein 7-X (W7-X, [73]). While the CBC case shows a broad, contiguous region of bad curvature with a monotonically decreasing profile of  $\mathcal{C}$ , the same is not true for the stellarator cases: NCSX has a non-monotonic profile of  $\mathcal{C}$  within a narrower region than CBC, while W7-X has multiple narrow regions of bad curvature separated by stabilising regions. This means there is no single parallel distance that cleanly separates destabilising from stabilising regions, and so it is not obvious that  $L_{\parallel}$  can be straightforwardly identified with a global quantity like the tokamak connection length. Indeed, clarifying what sets  $L_{\parallel}$  in stellarator turbulence remains an open problem, with recent work on critical-gradients [74], ITG-mode localisation [75], and other optimisation strategies [76–78] beginning to address this question.

We will therefore proceed by positing that there exists some well-defined  $L_{\parallel}$  — deferring the question of exactly how this is determined for a given equilibrium until §VC — and concentrate instead on the temperature-gradient scaling predicted by our asymptotic theory of §II. We assume, for now, that  $L_{\parallel}$  is a geometrical quantity that does not depend on the temperature gradient and so can be left aside for the purposes of this task, an assumption that we will confirm *a posteriori*. Now, the ETG predictions (24) relied on axisymmetry only through the identification of  $L_{\parallel}$  with the tokamak connection length; the assumption that the aspect ratio remains order unity,  $\mathcal{A}^o \sim 1$ , is likewise expected to hold in the stellarator case. Substituting this into (16) and choosing  $L_{\text{ref}} = a$ , where  $a$  is the minor radius at the last closed flux surface, we obtain

$$\frac{Q_e}{Q_{\text{gBe}}} \sim \left( \frac{L_{\parallel}}{a} \right) \left( \frac{a}{L_{T_e}} \right)^3, \quad k_y^o \rho_e \sim \frac{L_{T_e}}{L_{\parallel}}, \quad \mathcal{A}^o \sim 1. \quad (28)$$

This analogy is less straightforward for the ITG case, given that our scaling for  $\mathcal{A}^o$  in the case of tokamaks drew heavily on the toroidal secondary mechanism — a mode that has so far only been demonstrated in axisymmetric systems [26, 62]. Nevertheless, the underlying balance in (25) — between the outer-scale values of the ITG growth

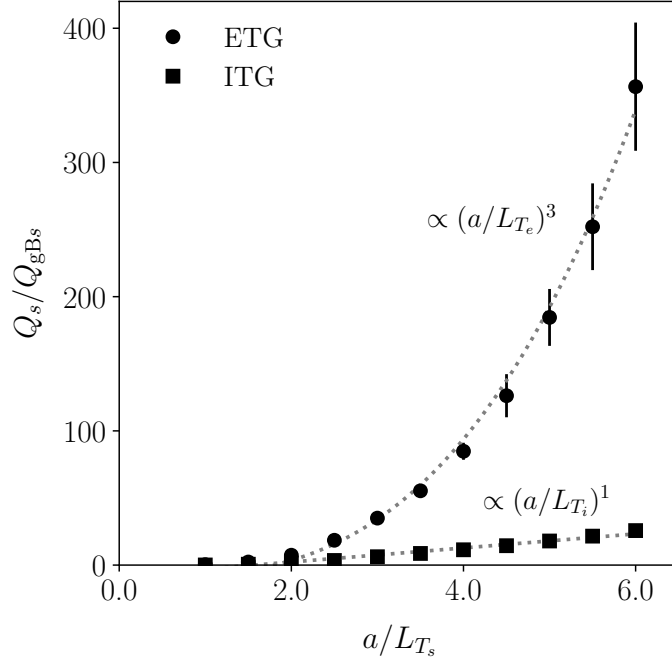


FIG. 8. Time-averaged gyro-Bohm normalised heat fluxes  $Q_s/Q_{gBs}$  from the NCSX simulations as functions of the normalised temperature gradients  $a/L_{T_s}$ , with the dotted lines showing the predicted scalings [first expressions in (24) and (26)] at large  $a/L_{T_s}$ . The circles and squares correspond to the ETG and ITG cases, respectively; the error bars show the standard deviation over time.

rate and the radial magnetic drift — is not inherently specific to tokamaks. The toroidal secondary emerges from a competition between zonal-flow shearing and the radial magnetic drifts, the physics that should remain in any toroidal system. Hence, although the specifics of the secondary mode may be modified in more complex stellarator fields, it is reasonable to posit, and test numerically, that a drift-regulated threshold for  $\mathcal{A}^\circ$  exists also in non-axisymmetric systems. Then our predictions for saturated ITG turbulence are [cf. (26)]:

$$\frac{Q_i}{Q_{gBi}} \sim \left( \frac{L_{\parallel}}{a} \right) \left( \frac{a}{R} \right)^2 \left( \frac{a}{L_{T_i}} \right), \quad k_y^o \rho_i \sim \frac{L_{T_i}}{L_{\parallel}}, \quad \mathcal{A}^\circ \sim \frac{R}{L_{\parallel}}. \quad (29)$$

It is evident from (28) and (29) that the axisymmetric results (24) and (26) arise as the special case obtained by setting  $L_{\parallel} = qR$ , as expected. In this sense, (28) and (29) represent the most general form of the ETG- and ITG-driven heat-flux scalings applicable to any toroidal geometry.

## B. NCSX simulations

To test our theory, we perform simulations of both ETG- and ITG-driven turbulence in NCSX geometry. We consider the flux-surface at mid-radius  $r/a = \sqrt{\psi/\psi_{LCFS}} = 0.5$ , where  $\psi_{LCFS}$  denotes the value of  $\psi$  at the last closed flux surface, and the  $\alpha = 0$  field line. The simulations once again evolve a single kinetic species, either electrons or ions, with the appropriate adiabatic closure applied. The normalised density gradient is fixed at  $a/L_{n_s} = 0.5$  throughout — chosen to maximise the heat flux at a given  $a/L_{n_s}$  [79] — while the normalised temperature gradient  $a/L_{T_s}$  is varied. The parallel simulation domain is extended for a single poloidal turn, viz.,  $\theta \in [-\pi, \pi]$ . Unless otherwise stated, all data are time-averaged over the last 80% of the simulation (see figure 16), with error bars indicating the standard deviation over the same interval. Further details of the numerical setup are given in §A.

The results of these scans in  $a/L_{T_s}$  for each species (labelled ‘NCSX ETG  $L_{T_e}$ ’ and ‘NCSX ITG  $L_{T_i}$ ’ in table I) are shown in figures 8 and 9. The heat fluxes (figure 8) closely follow the predicted cubic and linear scalings for ETG and ITG, respectively, while both the binormal outer scale and aspect ratio (figure 9) show good overall agreement with theoretical expectations. We were unable to obtain as large a range in  $a/L_{T_s}$  for the ITG simulations as in §IVB, owing to the fact that more than one poloidal turn was required in order to capture adequately the dynamics at such gradients [see panel (b) of figure 10], the computational cost of which proved prohibitively expensive. Even within

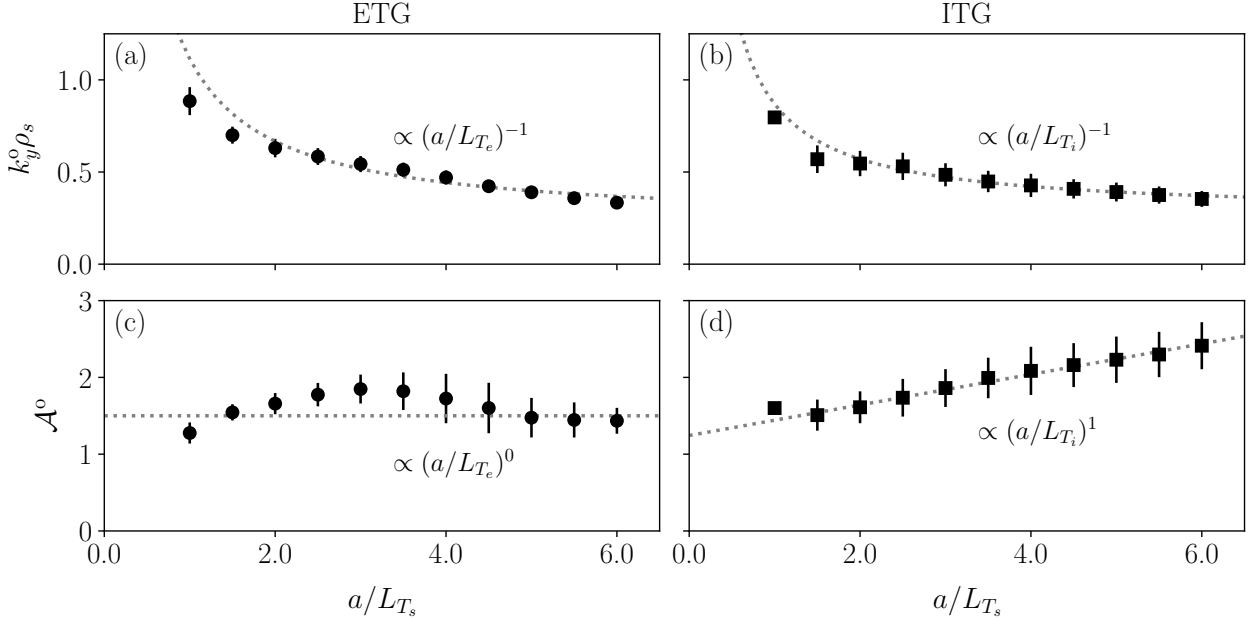


FIG. 9. Outer-scale binormal wavenumber and aspect ratio scalings from the same NCSX simulations as in figure 8. In all panels, the time-averaged values are indicated by the points, with circles corresponding to the ETG cases and squares to the ITG ones. The error bars show the standard deviation over time, while the dotted lines show the predicted scalings [second expressions in (28) and (29)]. (a) and (b):  $k_y^0 \rho_s$  as a function of the normalised temperature gradient  $a/L_{T_s}$  for ETG and ITG, respectively. (c) and (d):  $\mathcal{A}^0$  as a function of the normalised temperature gradient  $a/L_{T_s}$  for ETG and ITG, respectively.

this restricted range, however, the linear scaling of  $\mathcal{A}^0$  for ITG is clearly reproduced, as is evident from figure 9(d). Taken together, these results show that ETG and ITG turbulence follow the same  $a/L_{T_s}$  scalings as in the tokamak case, supporting the predictions (28) and (29).

That said, the theory with which we are claiming agreement rests on the assumption that there exists a well-defined  $L_{\parallel}$  for the underlying NCSX geometry that is independent of the temperature gradient. To assess the validity of this assumption, we examine directly the parallel structure of the turbulence in the set of simulations shown in figures 8 and 9. The results of this are summarised in figure 10. Panels (a) and (b) show the parallel spatial dependence of the heat flux [see (10)]

$$Q_s(z) = \sum_{k_x, k_y} Q_{s\mathbf{k}_{\perp}}(k_x, k_y, z). \quad (30)$$

Recall that we are using  $z = \theta$  as the parallel coordinate. For all values of the normalised temperature gradient, (30) has a maximum coinciding with the region of bad curvature localised in the outboard midplane ( $\theta = 0$ ), as one would expect from existing theories of the linear ITG modes in stellarators (see, e.g., [75]). While the information provided by  $Q_s(z)$  can be useful for, e.g., assessing the correspondence between values of the local magnetic curvature (27) and the magnitude of the heat flux at a given location along the field line, it is not necessarily the most appropriate quantity for determining the parallel system scale  $L_{\parallel}$ . Indeed, the causality argument proposed in §II E, which led to the binormal outer scale being determined in terms of the parallel system scale, implicitly assumed that  $L_{\parallel}$  was the parallel correlation length of the underlying turbulent fluctuations themselves, rather than the parallel length scale associated with the averaged quantity that is the heat flux. The more appropriate quantity from which to determine  $L_{\parallel}$  is therefore the two-point parallel correlation function of the non-zonal perturbed electrostatic potential:

$$G(z, z') = \frac{\text{Re} \left\langle \sum_{k_x, k_y \neq 0} \delta\phi_{\mathbf{k}_{\perp}}(z, t) \delta\phi_{\mathbf{k}_{\perp}}^*(z', t) \right\rangle_t}{\sqrt{\left\langle \sum_{k_x, k_y \neq 0} |\delta\phi_{\mathbf{k}_{\perp}}(z, t)|^2 \right\rangle_t} \sqrt{\left\langle \sum_{k_x, k_y \neq 0} |\delta\phi_{\mathbf{k}_{\perp}}(z', t)|^2 \right\rangle_t}}, \quad (31)$$

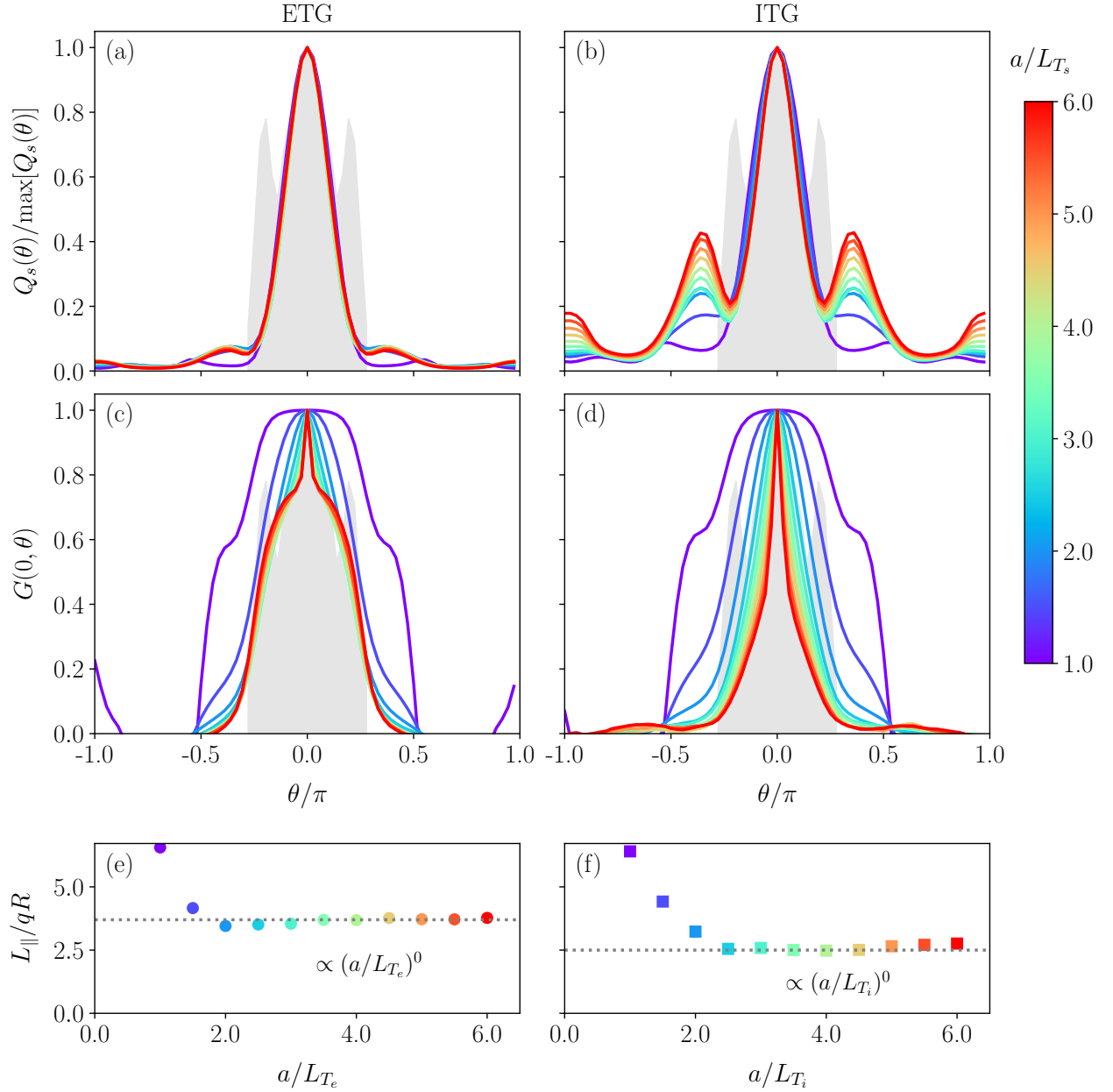


FIG. 10. Parallel structure of the turbulence from the same NCSX simulations as in figure 8, with the left and right columns corresponding to the ETG and ITG cases, respectively. In all panels, the colour indicates the value of the normalised temperature gradient  $a/L_{T_s}$ . The grey shaded regions in panels (a)-(d) are the area below the curve given by the negative of the local magnetic curvature (27) normalised to its maximum value, indicating the range of  $\theta$  in which the plasma is expected to be unstable. (a) and (b): time-averaged parallel spatial dependence of the heat flux (30) normalised to its maximum value. (b) and (c): parallel correlation function (31) of the fluctuations peaked at the outboard midplane ( $\theta = 0$ ). (e) and (f): the parallel system scale as determined from (33), viz.,  $L_{\parallel} = L_{\parallel}^{\text{corr}}(0)$ , normalised to the connection length  $qR$ , with circles corresponding to the ETG cases and squares to the ITG ones. The horizontal dotted lines indicate the expected scaling, i.e., that  $L_{\parallel}$  is independent of  $a/L_{T_s}$ .

where  $\langle \dots \rangle_t$  denotes an average over time. Note that, by definition,  $0 < G(z, z') \leq 1$ , with equality achieved at  $z = z'$ . This is plotted in panels (c) and (d) of figure 10. Except at the smallest values of the normalised temperature gradient, the parallel correlation function clearly retains the localisation around the region of bad curvature associated with the heat flux, but is significantly less peaked at larger values of  $\theta$ , particularly in the ITG case. Extracting the effective

width of the parallel correlation function

$$\Delta z(z) = \frac{\int_{-\infty}^{\infty} dz' |z - z'| |G(z, z')|}{\int_{-\infty}^{\infty} dz' |G(z, z')|} \quad (32)$$

one can then estimate the parallel correlation length:

$$L_{\parallel}^{\text{corr}}(z) = \int_{z-\Delta z}^{z+\Delta z} \frac{dz'}{|\mathbf{b} \cdot \nabla z'|}, \quad (33)$$

at a given  $z$  location. It is clear from panels (e) and (f) of figure 10 that the resultant parallel system scale evaluated at the outboard midplane,  $L_{\parallel}^{\text{corr}}(0)$ , is approximately independent of the normalised temperature gradient at all but the lowest values considered. This validates our *a priori* assumption that  $L_{\parallel}$  may be treated as independent of the temperature gradient in the heat-flux scalings (28) and (29) and, more importantly, demonstrates that strongly driven electrostatic turbulence in the NCSX equilibrium does indeed organise itself in accordance with the asymptotic scaling theory developed in §II, with the binormal outer scale being determined in terms of the parallel system scale.

### C. Determining the parallel system scale in CBC, NCSX, and W7-X equilibria

As stated previously, what sets the parallel system scale for stellarator equilibria remains a active subject of research. Although we will not attempt to resolve this question definitively, we here offer some discussion aimed at clarifying what ingredients a complete theory will ultimately need to capture, before providing a tentative answer informed by our numerical results.

We argued in §IV A that for axisymmetric equilibria, the parallel system scale is set by the inhomogeneity scale along the field line, corresponding to the width (in the parallel coordinate  $z$ ) of the bad-curvature region on the outboard side of the device. In stellarator equilibria, however, the complex distribution of good- and bad-curvature regions along a field line suggests that the parallel system scale could be determined in a qualitatively different way. Specifically, the proximity of the bad-curvature regions to one another along the field line (see, e.g., the curve labelled ‘W7-X’ in figure 7) raises the possibility that the turbulent fluctuations could remain correlated over several such regions, effectively extending the parallel system scale beyond what would be inferred from any single bad-curvature region, as in the tokamak. If this turns out to be the case, stellarator turbulence should be viewed not as being confined to an isolated unstable region, but as evolving on a spatially varying sequence of stabilising and destabilising curvature patches — a kind of ‘corrugated’ landscape on which the fluctuations live. In this picture, the effective parallel system scale would then have to reflect how fluctuations sample and respond to these alternating regions, and, in particular, how the turbulence remains correlated between them.

Distinguishing between these two possibilities cannot be done on the basis of our NCSX simulations alone due to the fact that, being a quasi-axisymmetric (QA), tokamak-like configuration, the equilibrium contains only a single bad-curvature region within a poloidal turn of the outboard midplane (see the curve labelled ‘NCSX’ in figure 7). Given that this is the only parallel inhomogeneity that was accessible to the turbulence in our simulations, it is unsurprising that the resulting parallel correlation length was roughly the same as the width of this bad-curvature region [see panels (c) and (d) of figure 10]. We therefore consider a further set of simulations for both ETG and ITG in the CBC, NCSX, and W7-X equilibria where the parallel simulation domain is extended for at least three poloidal turns, viz.,  $\theta \in [-3\pi, 3\pi]$ . The simulations once again evolve a single kinetic species, either electrons or ions, with the appropriate adiabatic closure applied. All simulations are conducted on a surface located at mid-radius  $r/a = 0.5$ , with the stellarator simulations done for the  $\alpha = 0$  field line. A normalised temperature gradient of  $a/L_{T_s} = 3.0$  is used throughout, while all other parameters such as the normalised density gradient  $a/L_{n_s}$ , magnetic shear  $\hat{s}$ , and safety factor  $q$  are the same as those used in sections §IV B and §V B, with the same gradients for the W7-X case as for the NCSX one. Unless otherwise stated, all data are time-averaged over the last 80% of each simulation’s running time (see figure 17). Further details of the numerical setup are given in §A.

The results of these simulations are summarised in figure 11. Each panel shows the time-averaged heat flux as a function of  $\theta$  (30) and the parallel correlation function (31) from an individual simulation, alongside shading indicating the bad-curvature regions [where  $\mathcal{C} < 0$ ; see (27)]. Considering first the CBC cases (top row), it is clear that there are contributions to the heat flux from each of the bad-curvature regions, as one would expect from an axisymmetric equilibrium. Furthermore, as we argued in §IV A, the correlation length of the fluctuations (33) is measured to be comparable to the width of these bad-curvature regions. As one might have guessed from the results of figure 10,

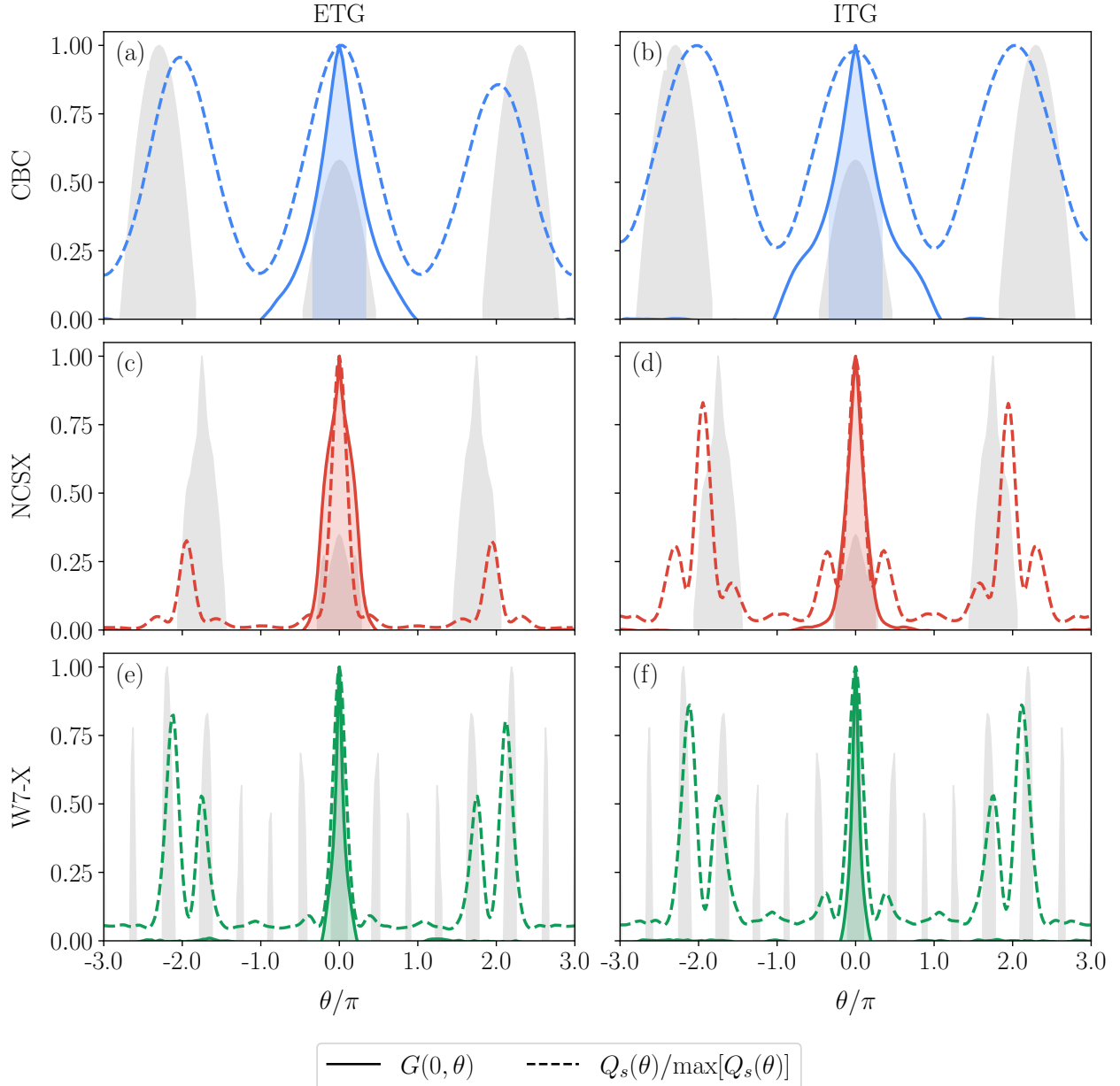


FIG. 11. Parallel structure of the turbulence from the simulations considered in §V C. The left and right columns correspond to the ETG and ITG cases, respectively, while the rows correspond to the given particular magnetic equilibrium: CBC (blue), NCSX (red), and W7-X (green), respectively (these colours are the same as those in figure 7). In all panels, the solid lines are the parallel correlation function (31) of the fluctuations peaked at the outboard midplane ( $\theta = 0$ ), while the dashed lines are the time-averaged parallel spatial dependence of the heat flux (30) normalised to its maximum value. The shaded coloured regions below the former indicate a region of width given by the parallel system scale as determined from (33), viz.,  $L_{\parallel} = L_{\parallel}^{\text{corr}}(0)$ , while the grey shaded regions are the areas below the curve given by the negative of the local magnetic curvature (27) normalised to its maximum value, indicating the range of  $\theta$  in which the plasma is expected to be unstable.

the behaviour of the turbulence in the NCSX cases (middle row) is entirely analogous to the CBC cases, with its correlation length again comparable to the width of the central bad-curvature region. Interestingly, and perhaps disappointingly, the turbulence in the W7-X cases (bottom row) displays similar behaviour. Despite there being five distinct bad-curvature regions within a single poloidal turn of the outboard midplane that contribute to the heat flux, the correlation length of the turbulence is not significantly larger than in the CBC and NCSX cases, spanning only the central bad-curvature region. The same is also true when considering the correlation function at different locations along the field line, viz., for different values of  $\theta'$  in  $G(\theta', \theta)$ , as can be seen in figure 12.

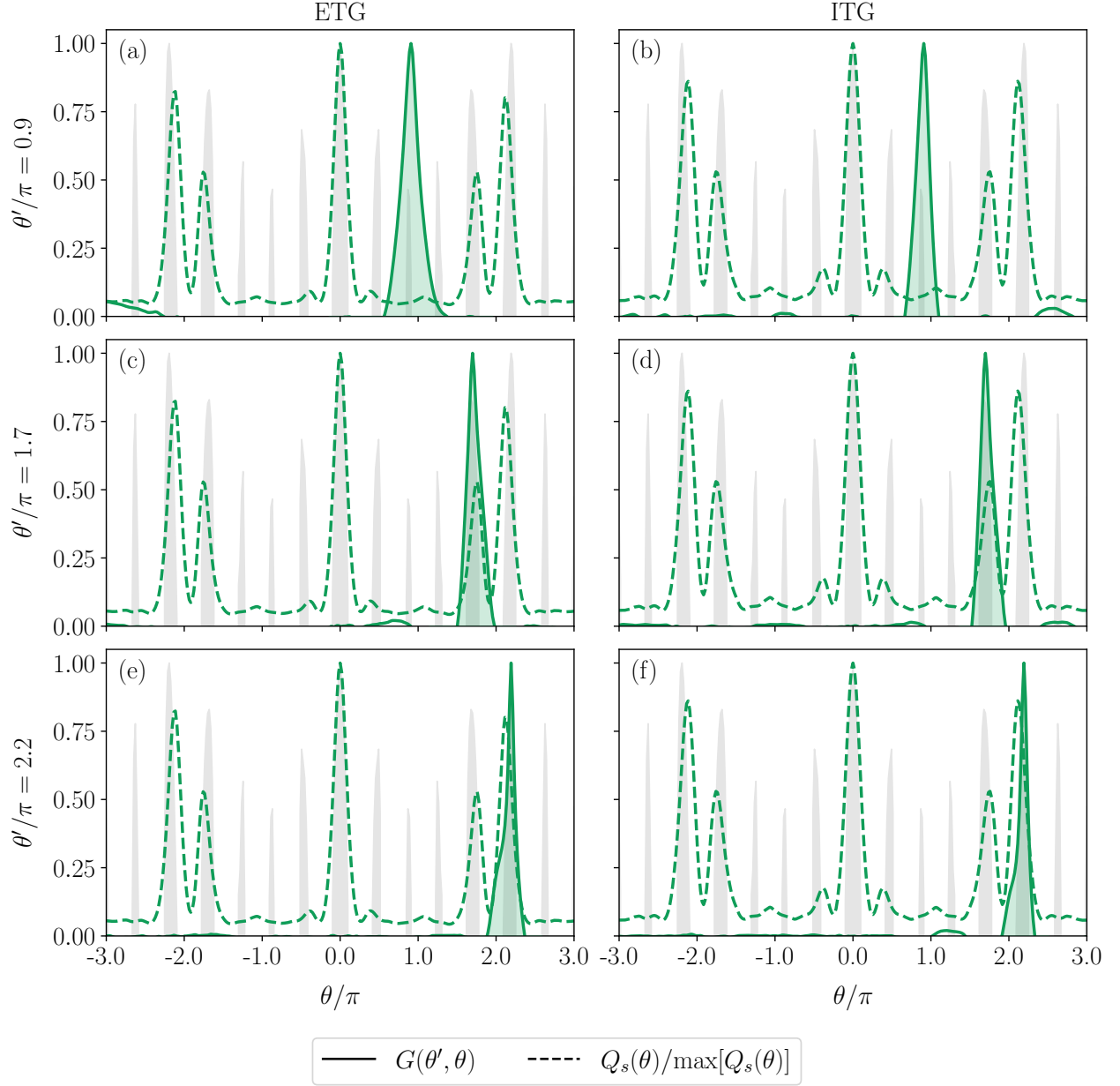


FIG. 12. The same as figure 11, except the rows now show the parallel correlation function (31) for fluctuations at different locations along the field line (solid lines) in the W7-X simulations.

These results suggest that the physics that determines the parallel system scale in stellarator turbulence is not qualitatively different to that encountered in axisymmetric geometries: in both cases, the turbulent fluctuations only remain correlated over a small width in the parallel coordinate  $z$ , corresponding to local bad-curvature regions. This means that the parallel system scale is still set by the scale of the inhomogeneity along the field line. Given, however, that stellarator field lines typically encounter multiple bad-curvature regions of comparable size distributed along  $z$ , this scale cannot be identified with the width of any single region at a particular location. Instead, it should be understood as some average measure of the length of the bad-curvature regions on a given field line, e.g., the following measure of the effective parallel system scale:

$$L_{\parallel}^{\text{eff}} = \left\langle \int_{z-\pi}^{z+\pi} \frac{dz'}{|\mathbf{b} \cdot \nabla z'|} H[-\mathcal{C}(z')] \right\rangle_z, \quad (34)$$

where  $H$  is the Heaviside step function and  $\mathcal{C}$  is as defined in (27). The integral appearing in (34) measures the physical length of the bad-curvature regions along the field line within a  $2\pi$  width (e.g., within a toroidal or poloidal turn) of a given location in  $z$ . Averaging over these locations then yields a global measure of the parallel system scale that is insensitive to the local starting point. Determining whether estimates such as (34) are an effective measure of the parallel system scale across a wide array of magnetic equilibria is the subject of ongoing work.

An interesting feature of our results is the fact that the parallel correlation function — and hence the resulting parallel system scale — differs between ETG- and ITG-driven turbulence (see figures 10, 11, and 12). In particular, the parallel correlation length of ETG-driven turbulence is systematically larger than that of its ITG-driven counterpart, with the difference being most pronounced in the NCSX equilibrium [compare, for example, panels (e) and (f) of figure 11]. Since the only distinction between the ETG- and ITG-driven simulations considered in this paper is the form of the adiabatic response of the non-driving species, this disparity in correlation lengths is most naturally attributed to differences in zonal-flow dynamics. A more detailed understanding of how zonal flows modify the parallel structure of the turbulence would therefore be required to refine (34) so as to account explicitly for species-dependent effects, given that the present estimate is agnostic to which species is treated kinetically.

A more important limitation to our conclusions here is due to the nature of the local flux-tube approximation. In particular, our nonlinear simulations of NCSX and W7-X were restricted to the  $\alpha = 0$  field line on the chosen flux surface, even though the turbulence may differ elsewhere on the same surface. Local studies of stellarator turbulence will sometimes attempt to account for this possible variation by performing nonlinear simulations for a number of different values of  $\alpha$  and averaging the resultant turbulent statistics. However, this approach implicitly assumes that the zonal flows determined locally in one flux-tube domain are consistent with those in others — an assumption that is highly restrictive and almost certainly violated in realistic stellarator equilibria [80–82]. More faithful treatment of the zonal dynamics — and hence of the saturation level of ITG turbulence, given the role of the toroidal secondary in the axisymmetric limit — may ultimately require simulations that are global in  $\alpha$  (while remaining local in  $\psi$ ), an approach currently under active investigation [83].

With these caveats acknowledged, however, our results strongly suggest that the scaling behaviour captured in (28) and (29) is already manifest in conventional flux-tube stellarator turbulence. This makes the present work a useful reference point for future poloidally global studies, and a first confirmation that the asymptotic theory developed in §II provides the right framework for interpreting stellarator turbulence and developing a more complete theory for the parallel system scale  $L_{\parallel}$ .

## VI. SUMMARY AND DISCUSSION

Using simple physical arguments about the nature of the competition between the various time scales appearing in temperature-gradient-driven electrostatic gyrokinetic turbulence — viz., rates of linear growth, nonlinear decorrelation, and parallel propagation — we have constructed a general theory for the asymptotic scaling of the heat flux with the normalised temperature gradient and other parameters of the magnetic equilibrium (§II). Two quantities emerged as central to this theory: the parallel system scale  $L_{\parallel}$  and the outer-scale aspect ratio  $\mathcal{A}^o = k_x^o/k_y^o$ , which together set the scaling of the heat flux.

While the exact form of the parallel system scale depended on the specific magnetic equilibrium — the parallel size of the box in a uniform magnetic field (§III) or the connection length  $L_{\parallel} \sim qR$  in an axisymmetric toroidal one (§IV) — we argued that the outer-scale aspect ratio was not controlled by the geometry directly. Instead, the key factor that determined  $\mathcal{A}^o$  was the nature of the response of the other plasma species, assumed adiabatic. For ETG, the adiabatic ion response (17) provides no mechanism to enforce a strong anisotropy between the radial and binormal directions, leading to  $\mathcal{A}^o \sim 1$ , independent of the electron temperature gradient  $L_{T_e}$ . For ITG, by contrast, the modified adiabatic electron response (18) explicitly privileges zonal-flow dynamics, giving rise to the ‘toroidal secondary’ [26, 62]. This mode acts to limit the aspect-ratio of ITG turbulence by destabilising structures above a certain threshold in aspect ratio, thus causing it to scale with the temperature gradient as  $\mathcal{A}^o \sim R/L_{T_i}$ . Together, these differences imply that ETG-driven core turbulence has an asymptotic scaling with the temperature gradient that is much stiffer than its ITG-driven counterpart, viz., in a toroidal system with minor radius  $a$ ,

$$\frac{Q}{Q_{\text{gBs}}} \sim \frac{L_{\parallel}}{a} \begin{cases} \left(\frac{a}{L_{T_e}}\right)^3, & \text{ETG,} \\ \left(\frac{a}{L_{T_i}}\right)^1 \left(\frac{a}{R}\right)^2, & \text{ITG.} \end{cases} \quad (35)$$

where  $Q_{\text{gBs}} = n_s T_s v_{\text{th}s} (\rho_s/a)^2$  is the gyro-Bohm heat flux. We have confirmed these scalings using nonlinear gyrokinetic simulations in a slab (for ETG), CBC [50, 69], and NCSX [72] magnetic equilibria (§III B, §IV B, and §V B, respectively). Notably, this is the first numerical confirmation of the cubic heat-flux scaling with the temperature gradient in ETG-driven turbulence, anticipated from earlier theoretical work [25, 29]. In the CBC case, we also verified the scaling with the connection length  $L_{\parallel} \sim qR$ , as had previously been demonstrated for ITG turbulence [24, 26]. Although determining a general expression for  $L_{\parallel}$  in stellarator magnetic fields remains an active area of research, the results of §V suggest that the physics determining the parallel system scale in stellarator turbulence is not qualitatively different to that encountered in tokamaks, with the turbulent fluctuations only remaining correlated over local bad-curvature regions in both cases. As such, the consistency of the observed scalings across both axisymmetric and non-axisymmetric configurations underscores the generality of the asymptotic scaling theory developed in §II.

A direct implication of (35) is that one would expect electrostatic turbulent transport to be stiffer should it be dominated by the electron channel, which can occur, e.g., when ITG is suppressed by strong  $\mathbf{E} \times \mathbf{B}$  shear in steep-gradient regions of a tokamak (e.g., the pedestal), particularly in spherical or low-aspect-ratio configurations (see, e.g., [19–23] and references therein). In such contexts, the cubic scaling of ETG turbulence implies that modest increases in the temperature gradient can trigger disproportionately large increases in transport. Moreover, [59] demonstrated that at gradients well beyond those considered here, ETG transport can become even stiffer, finding empirically that the heat flux scaled quartically with the temperature gradient. This stronger scaling arises from the localisation of ETG modes along the field line (i.e., away from  $\theta = 0$ ), caused by the combined effects of magnetic drifts and finite-Larmor-radius corrections at large drive. In the present context, this can be conceptualised in terms of a modification of  $L_{\parallel}$  in such steeper-gradient regions: balancing the diamagnetic and magnetic drifts, one can show that  $L_{\parallel} \sim (qR/\dot{s})(R/L_{T_e})$  [see equation (41) of [58] and the surrounding discussion], allowing for the quartic scaling to be recovered directly from (35) if  $L_{\parallel}$  is allowed to depend on gradients of the plasma equilibrium. This behaviour has important implications for reactor design and operation: if electron-channel transport dominates, the strong nonlinearity of ETG scaling could make pedestal performance highly sensitive to small changes in gradients, complicating both predictive modelling and experimental control [84, 85].

The scalings (35) also have interesting implications for the relative importance of ETG and ITG transport as a function of the device aspect ratio  $R/a$ . Estimating the ratio of the ion to electron heat fluxes under the assumptions  $n_i \sim n_e$ ,  $T_i \sim T_e$ , and  $L_{T_i} \sim L_{T_e} \sim a$ , we find that the electron channel dominates once  $R/a \gtrsim (m_i/m_e)^{1/4} \approx 7.8$ . This threshold lies well above the aspect ratios envisioned for reactor-relevant tokamaks, such as ITER with  $R/a = 3.1$  [86, 87], but is directly relevant for recent stellarator designs, which are targeting substantially larger values  $R/a \gtrsim 10$  [see, e.g., 88, 89]. This raises the possibility that in high-aspect ratio stellarators, confinement could be limited primarily by ETG turbulence rather than ITG. Motivated by comparisons to W7-X experimental data [90, 91], most stellarator turbulence studies to date have focussed on ITG as the dominant transport channel (note, however, [92, 93]). If ETG transport becomes comparable to, or even larger than, ITG transport as  $R/a$  increases, optimisation strategies may need to shift accordingly, especially if the ion-scale turbulence is so well optimised that it does not significantly suppress the ETG-scale turbulence through cross-scale interactions (see §VII B for further discussion). In particular, greater emphasis would be required on how the parallel system scale  $L_{\parallel}$  and field-line geometry shape electron-scale dynamics. These considerations suggest that the role of ETG transport in large-aspect-ratio stellarators is a key open question, with potentially important implications for future optimisation efforts.

To conclude, this work shows that a remarkably simple asymptotic theory, built only from considering the competition of a few fundamental time scales, can successfully explain the behaviour of both ETG- and ITG-driven electrostatic turbulence. The numerical results presented here therefore do more than confirm a set of asymptotic scalings: they provide a foundation for physics-based reduced models of turbulent transport that can be used to inform reactor design. Existing transport models employed in optimisation studies often rely on linear gyrokinetic theory, which can be a poor predictor of nonlinear performance, or on expensive nonlinear gyrokinetic calculations, which can be difficult to deploy systematically across wide regions of parameter space. By contrast, the asymptotic theory developed here isolates the essential balances that control ETG- and ITG-driven transport, distilling from gyrokinetics a pair of physically transparent parameters: the outer-scale aspect ratio  $\mathcal{A}^o$  and the parallel system scale  $L_{\parallel}$ . While our results suggest that  $\mathcal{A}^o$  is a quantity insensitive to the details of magnetic geometry, the parallel system scale  $L_{\parallel}$  must ultimately be set, at least in part, by that geometry. In tokamaks, this connection is well understood, but in stellarators, its precise determination remains an open problem, making it the key link between geometry and transport. Nevertheless, the fact that our framework reduces turbulent transport to a dependence on just  $L_{\parallel}$  and  $\mathcal{A}^o$  means it offers a tractable pathway for building reduced, geometry-aware models that can accelerate stellarator optimisation and guide the design of future reactors.

## VII. OPEN ISSUES

While the results of this paper show that the theory developed here is broadly general (e.g., being agnostic to the choice of magnetic equilibrium), we necessarily introduced a number of simplifications in order to make analytical progress. Such simplifications, however, always come at a cost to general applicability, and so we will here devote some space to a discussion of the most pressing lines of investigation left open by this work.

### A. Near-marginal regime

One key assumption of §II was that the turbulence was sufficiently strongly driven that it sat far from marginality, i.e., at gradients sufficiently far above either the linear critical gradient or, in the case of ITG turbulence, the Dimits threshold [50]. In the latter case, the reason for this is obvious: the dynamics below the Dimits threshold is regulated by strong, long-lived, large-scale zonal flows [47, 49, 64, 68, 94, 95], representing an entirely different type of turbulence than considered here. At first sight, this restriction to large gradients might appear to limit the applicability of our theory, since much of fusion-relevant plasma is expected to sit at or close to the high-transport threshold. However, the results derived under the assumption of strong drive must still connect continuously to the near-threshold state, provided that the heat flux is a continuous function of the equilibrium gradients. For example, transport models developed for ETG turbulence in the tokamak pedestal often parametrise the heat flux as (cf. [70, 85, 96])

$$Q_e \propto \left( \frac{a}{L_{T_e}} \right)^2 \left( \frac{a}{L_{T_e}} - \frac{a}{L_{T_e}^{\text{crit.}}} \right)^\lambda, \quad (36)$$

where  $L_{T_s}^{\text{crit.}}$  is some (linear or nonlinear) critical gradient and  $\lambda$  a constant. This reproduces our predicted cubic scaling at gradients much larger than  $L_{T_e}^{\text{crit.}}$  if  $\lambda = 1$ , which is close to the values obtained from simulations based on experimental data [70, 85]. Models similar to (36) have also been employed to describe ITG-driven core turbulence (see, e.g., [97, 98]). In this sense, our results can be interpreted as the ‘universal’ asymptotic behaviour of electrostatic gyrokinetic turbulence above threshold, to which near-marginal states must connect. Indeed, the predicted scalings were observed already for gradients only a factor of order unity above the linear critical values [see figure 3(a) and figure 8], suggesting that extreme drive is not required for the scalings to manifest. This could make the theory particularly valuable for constructing reduced, physics-based transport models: it identifies the fundamental physical scalings that persist from the strongly driven limit into regimes close to marginality.

### B. Effect of cross-scale interactions

The theory developed in §II was constructed for turbulence driven by a single species (either electrons or ions) — with the other species treated as adiabatic through the appropriate closure — in order to isolate the fundamental dynamics underpinning the turbulence. This, however, is only an approximation: any realistic fusion plasma necessarily contains at least four kinetic species (deuterium, tritium, electrons, alphas), and their coupled dynamics can in principle alter both the drive and saturation mechanisms of the turbulence.

For ion-scale dynamics, the modified adiabatic electron closure (18) is predicated on the assumption of (infinitely) fast parallel electron streaming, viz., that the electrons will sample the entire flux surface in a single dynamical time. Since the nonlinear decorrelation rate of the most energetic ion-scale fluctuations is comparable to the ions’ parallel-streaming rate [see (14)], this approximation remains accurate to leading order in the square-root of the electron-ion mass ratio  $\sqrt{m_e/m_i}$ . Nevertheless, retaining kinetic electrons can give rise to additional ion-scale instabilities, such as trapped-electron modes [99–102], which are often considered to be an important source of turbulent fluctuations and have been the focus of some schemes for optimising stellarator configurations [103–105]. These instabilities, however, typically operate on scales smaller than those at which the heat flux peaks in our nonlinear ITG simulations. Given that the largest scales tend to give the dominant contributions to the heat flux, we conjecture that our results will not be substantially altered for ITG-driven (rather than TEM-driven) turbulence in the presence of kinetic electrons, though it is up to future work to determine whether this is indeed the case.

In the case of ETG-driven turbulence, the adiabatic ion closure does not rely on a time scale separation, but rather on a length-scale separation between the ion-Larmor radius and the characteristic wavenumbers of the fluctuations,  $k_\perp \rho_i \gg 1$ . However, given the scaling of the binormal outer scale  $k_y^o \rho_e \sim L_{T_e}/L_\parallel$  [see (28)], the dominant injection scale shifts towards progressively larger values as the temperature gradient increases. At sufficiently large gradients, this binormal scale could approach the ion Larmor radius, at which point the effects of kinetic ions can no longer be

neglected. Assuming  $T_i \sim T_e$ , this crossover occurs when  $L_{\parallel}/L_{T_e} \sim qR/L_{T_e} \sim \sqrt{m_i/m_e}$ . While such values are much higher than those typically realised in the core, they are comparable to gradients expected in the edge and pedestal regions (see, e.g., [59]), implying that ETG turbulence in these regimes certainly requires a fully kinetic treatment of both species.

Numerically expensive gyrokinetic simulations with enough resolution to span both ion and electron scales have shown that ion-scale turbulence can directly suppress electron-scale fluctuations [106–109], with experimental results supporting this possibility [110]. This effect is attributed to the ion-scale turbulence providing strong  $\mathbf{E} \times \mathbf{B}$  shear flows that break up the turbulent electron-scale eddies, either in the perpendicular plane or via the parallel-to-the-field  $\mathbf{E} \times \mathbf{B}$  shearing mechanism proposed by [111]. It is worth emphasising that, unlike the breakdown of the adiabatic-electron approximation described in the previous paragraph, such cross-scale suppression of ETG does not require large gradients to manifest, and so further work will be required to determine whether our results are robust to such considerations, even at the comparatively modest gradients used in our simulations.

### C. Electromagnetic fluctuations

We have restricted our analysis to electrostatic turbulence, in which the dynamics are mediated only through the perturbed electrostatic potential  $\delta\phi$  [see (2) and (3)]. Reactor-relevant tokamak and stellarator plasmas, however, will generally operate at finite beta, where magnetic-field fluctuations cannot be ignored. This not only introduces additional linear instabilities — most prominently the microtearing (MTM [112–121]) and kinetic-ballooning (KBM [21, 122–138]) modes — but can also change the way in which those instabilities localise along field lines [33, 120]. In particular, while KBMs remain tied to bad-curvature regions, MTMs can extend more broadly, meaning that both the critical-balance estimate (14) and the identification  $L_{\parallel} \sim qR$  may need to be revisited in electromagnetic regimes. Moreover, finite fluctuations in the parallel magnetic-vector potential  $\delta A_{\parallel}$  and magnetic-field strength  $\delta B_{\parallel}$  are expected to play a direct role in mediating outer-scale injection. For example, such electromagnetic fluctuations introduce more nonlinear terms into the gyrokinetic system of equations, meaning that the assumption that the nonlinear decorrelation rate is set by the (electrostatic)  $\mathbf{E} \times \mathbf{B}$  shearing one (7) may have to be modified. Developing a full scaling theory that includes these electromagnetic effects remains an open challenge, with tentative predictions already proposed by [25], but one of central importance for predictive modelling of transport in next-generation devices. The present results provide a necessary electrostatic baseline from which such extensions can be built.

## ACKNOWLEDGEMENTS

The authors would like to thank G. Acton, S. C. Cowley, G. W. Hammett, and R. Nies for helpful discussions and suggestions at various stages of this project.

## FUNDING

This work was supported in part by the Engineering and Physical Sciences Research Council (EPSRC) [EP/R034737/1 and EP/W006839/1]. The work of T.A. was supported in part by the Laboratory Directed Research and Development (LDRD) Program at the Princeton Plasma Physics Laboratory for the U.S. Department of Energy under Contract No. DE-AC02-09CH11466. The United States Government retains a non-exclusive, paid-up, irrevocable, world-wide license to publish or reproduce the published form of this manuscript, or allow others to do so, for United States Government purposes. The work of S.B. was supported by a grant from the Simons Foundation/SFARI (560651, AB) and the Department of Energy Award No. DE-SC0024548 (until March 31, 2025). The work of I.G.A was supported by US Department of Energy grants DE-FG0293ER54197, DE-SC0018429, and DE-SC0024425. The work of M.B. and A.A.S. was supported in part by the EPSRC grant EPR034737/1; the work of A.A.S. was also supported in part by the Simons Foundation via a Simons Investigator award. The authors acknowledge the support of the Royal Society Te Apārangi, through Marsden-Fund grant MFP-UOO2221 (T.A. and J.S.) and MFP-U0020 (R.M.). The work of R.M. was also supported in part by NASA grant 80NSSC24K0171. This research used resources of the National Energy Research Scientific Computing Center (NERSC), a Department of Energy User Facility using NERSC awards FES-ERCAP-0032464 and FES-ERCAP-0031087. Some of the simulations presented in this article were performed on computational resources managed and supported by Princeton University's Research Computing, and on the HPC systems Raven & Viper at the Max Planck Computing and Data Facility.

	$N_{\text{pol}}$	$L_{\text{ref}}/L_{T_s}$	$L_{\text{ref}}/L_{n_s}$	$q$	$L_x/\rho_s$	$L_y/\rho_s$	$N_{\parallel}$	$N_x$	$N_y$	$N_m$	$N_l$	$D_{\text{hyper}}$	Sims.
sETG	—	1.00	0.00	—	444	444	(12, 128)	216	216	24	6	0.05	11
CBC ETG $L_{T_e}$	1.0	(1.50, 6.00)	0.80	2.80	354	444	48	486	512	12	6	0.10	10
CBC ITG $L_{T_i}$	1.0	(2.00, 15.0)	0.80	2.80	354	444	48	486	512	12	6	0.10	14
CBC ETG $q$	1.0	2.00	0.80	(0.70, 7.00)	354	444	64	384	512	12	6	0.10	19
	1.0	2.50	0.80	(0.70, 7.00)	354	444	64	384	512	12	6	0.10	19
	1.0	5.00	0.80	(0.70, 7.00)	354	444	64	384	512	12	6	0.10	19
CBC ITG $q$	1.0	2.00	0.80	(0.70, 7.00)	442	444	16	1024	432	8	12	0.10	19
	1.0	2.50	0.80	(0.70, 7.00)	442	444	16	1024	432	8	12	0.10	19
	1.0	5.00	0.80	(0.70, 7.00)	442	444	16	1024	432	8	12	0.10	19
NCSX ETG $L_{T_e}$	1.0	(1.00, 6.00)	0.50	2.06	587	444	72	648	512	16	6	0.10	11
NCSX ITG $L_{T_i}$	1.0	(1.00, 6.00)	0.50	2.06	587	444	72	648	512	16	6	0.10	11
CBC ETG $L_{\parallel}$	3.0	3.00	0.80	2.80	237	222	144	324	256	12	6	0.10	1
CBC ITG $L_{\parallel}$	3.0	3.00	0.80	2.80	237	222	144	324	256	12	6	0.10	1
NCSX ETG $L_{\parallel}$	3.0	3.00	0.50	2.06	244	222	216	324	256	16	6	0.10	1
NCSX ITG $L_{\parallel}$	3.0	3.00	0.50	2.06	244	222	216	324	256	16	6	0.10	1
W7-X ETG $L_{\parallel}$	3.2	3.00	0.50	1.14	240	222	324	324	256	12	6	0.10	1
W7-X ITG $L_{\parallel}$	3.2	3.00	0.50	1.14	240	222	324	324	256	12	6	0.10	1

TABLE I. The numerical parameters used for the gyrokinetic simulations considered in this paper. Values in parentheses indicate the minimum and maximum values for the corresponding column, with the final column ('sims') indicating the number of simulations in a given set. A dash in an entry indicates that the given simulation does not take that parameter as an input.

### DECLARATION OF INTERESTS

I.G.A. is a co-founder and owner of GridFire Inc., a private fusion company.

### Appendix A: Numerical details

All simulations in this paper were performed with the gyrokinetic code [GX](#) [7], for which the relevant numerical input parameters are detailed in table I. The quantities  $L_x$  and  $L_y$  denote the box sizes in the radial and binormal directions, respectively, and are related to the associated minimum wavenumber by  $k_{x,y}^{\min} = 2\pi/L_{x,y}$ . The spatial resolution is determined by  $N_{\parallel}$ , the number of (equal-arc) parallel grid points, as well as  $N_x$  and  $N_y$ , the numbers of Fourier modes in the radial and binormal directions, respectively. The velocity-space resolution is determined by the number of Hermite moments  $N_m$  (dual to the parallel velocity) and Laguerre moments  $N_l$  (dual to the magnetic moment). Perpendicular hyperviscosity of the form  $\propto k_{\perp}^4$  is employed to remove energy at the grid scale in perpendicular-wavenumber space. The strength of this dissipation is controlled by  $D_{\text{hyper}}$ . A small amount of physical collisions,  $(L_{\text{ref}}/v_{\text{th}s})\nu_{ss} \approx 0.01$  — in addition to ‘hypercollisions’ (using the standard implementation in [GX](#), see [7]) — were included to provide a sufficient sink of energy at small scales in velocity space. Resolution studies were performed in all of these parameters to ensure numerical convergence. The flux-tube simulations shown in sections IV B and V B were extended for a single poloidal turn ( $N_{\text{pol}} = 1.0$ ), while those in §V C were extended for three or more poloidal turns ( $N_{\text{pol}} \geq 3.0$ ). Standard or generalised ‘twist-and-shift’ boundary conditions [32, 139] were used in all cases. All simulations were run for at least 2000 normalised time units, with the sETG simulations (see §III) having been run for at least 30000 in order to have adequate statistics for time-averaging.

### Appendix B: Supplementary simulation data

In this appendix, we include supplementary data from the simulations presented in §IV B (figs. 13 to 15), §V B (figure 16), and §V C (figure 17). These results are included for completeness and to aid readers interested in the data underlying the time-averaged values shown in the main text. Where shown, dotted lines indicate the scalings predicted by previous theories of the inertial range [24, 25, 30]. We emphasise, however, that the asymptotic scaling theory developed in §II does not rely on agreement with these predictions, remaining agnostic to whether or not they are realised in practice.

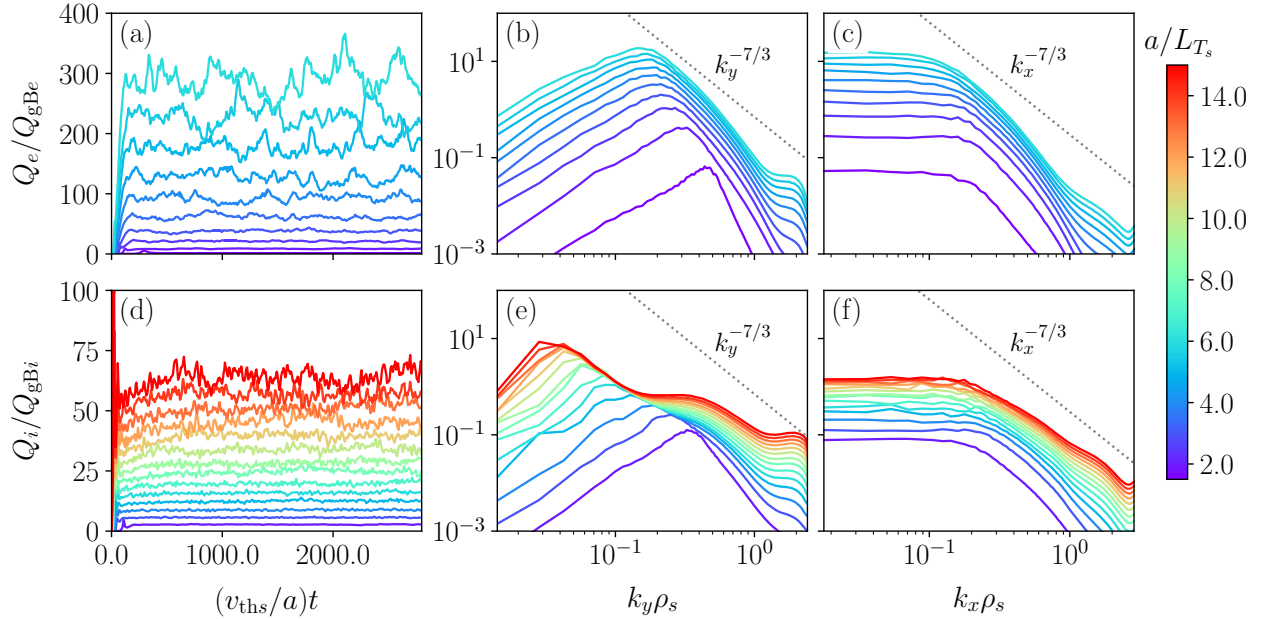


FIG. 13. Data from the simulations labelled ‘CBC ETG  $L_{T_e}$ ’ and ‘CBC ITG  $L_{T_i}$ ’ in table I, shown in the top and bottom rows, respectively. The colours indicate the value of  $a/L_{T_s}$  for the given simulation, and all data shown is normalised to  $Q_{gBs} = n_s T_s v_{th}s (\rho_s/a)^2$ . First column: heat fluxes as functions of time. Second column: time-averaged one-dimensional binormal heat-flux spectra (22). Third column: time-averaged one-dimensional radial heat-flux spectra (23).

---

[1] E. A. Frieman and L. Chen, Nonlinear gyrokinetic equations for low-frequency electromagnetic waves in general plasma equilibria, *Phys. Fluids* **25**, 502 (1982).

[2] I. G. Abel, G. G. Plunk, E. Wang, M. Barnes, S. C. Cowley, W. Dorland, and A. A. Schekochihin, Multiscale gyrokinetics for rotating tokamak plasmas: fluctuations, transport and energy flows, *Rep. Prog. Phys.* **76**, 116201 (2013).

[3] P. J. Catto, Practical gyrokinetics, *J. Plasma Phys.* **85**, 925850301 (2019).

[4] M. Kotschenreuther, G. Rewoldt, and W. M. Tang, Comparison of initial value and eigenvalue codes for kinetic toroidal plasma instabilities, *Comp. Phys. Comms.* **88**, 128 (1995).

[5] F. Jenko, Massively parallel Vlasov simulation of electromagnetic drift-wave turbulence, *Comp. Phys. Comms.* **125**, 196 (2000).

[6] J. Candy, E. A. Belli, and R. V. Bravenec, A high-accuracy Eulerian gyrokinetic solver for collisional plasmas, *J. Comp. Phys.* **324**, 73 (2016).

[7] N. R. Mandell, W. Dorland, I. Abel, R. Gaur, P. Kim, M. Martin, and T. Qian, GX: a GPU-native gyrokinetic turbulence code for tokamak and stellarator design, *J. Plasma Phys.* **90**, 905900402 (2024).

[8] G. M. Staebler, J. E. Kinsey, and R. E. Waltz, A theory-based transport model with comprehensive physics, *Phys. Plasmas* **14**, 055909 (2007).

[9] G. M. Staebler and J. E. Kinsey, Electron collisions in the trapped gyro-Landau fluid transport model, *Phys. Plasmas* **17**, 122309 (2010).

[10] C. Bourdelle, X. Garbet, F. Imbeaux, A. Casati, N. Dubuit, R. Guirlet, and T. Parisot, A new gyrokinetic quasilinear transport model applied to particle transport in tokamak plasmas, *Phys. Plasmas* **14**, 112501 (2007).

[11] C. Bourdelle, J. Citrin, B. Baiocchi, A. Casati, P. Cottier, X. Garbet, F. Imbeaux, and the JET Contributors, Core turbulent transport in tokamak plasmas: bridging theory and experiment with QuaLiKiz, *Plasma Phys. Control. Fusion* **58**, 014036 (2016).

[12] C. S. Liu, Instabilities in a magnetoplasma with skin current, *Phys. Rev. Lett.* **27**, 1637 (1971).

[13] Y. C. Lee, J. Q. Dong, P. N. Guzdar, and C. S. Liu, Collisionless electron temperature gradient instability, *The Physics of Fluids* **30**, 1331 (1987).

[14] W. Dorland, F. Jenko, M. Kotschenreuther, and B. N. Rogers, Electron temperature gradient turbulence, *Phys. Rev. Lett.* **85**, 5579 (2000).

[15] F. Jenko, W. Dorland, M. Kotschenreuther, and B. N. Rogers, Electron temperature gradient driven turbulence, *Phys. Plasmas* **7**, 1904 (2000).

[16] R. E. Waltz, Three-dimensional global numerical simulation of ion temperature gradient mode turbulence, *Phys. Fluids* **31**, 1962 (1988).

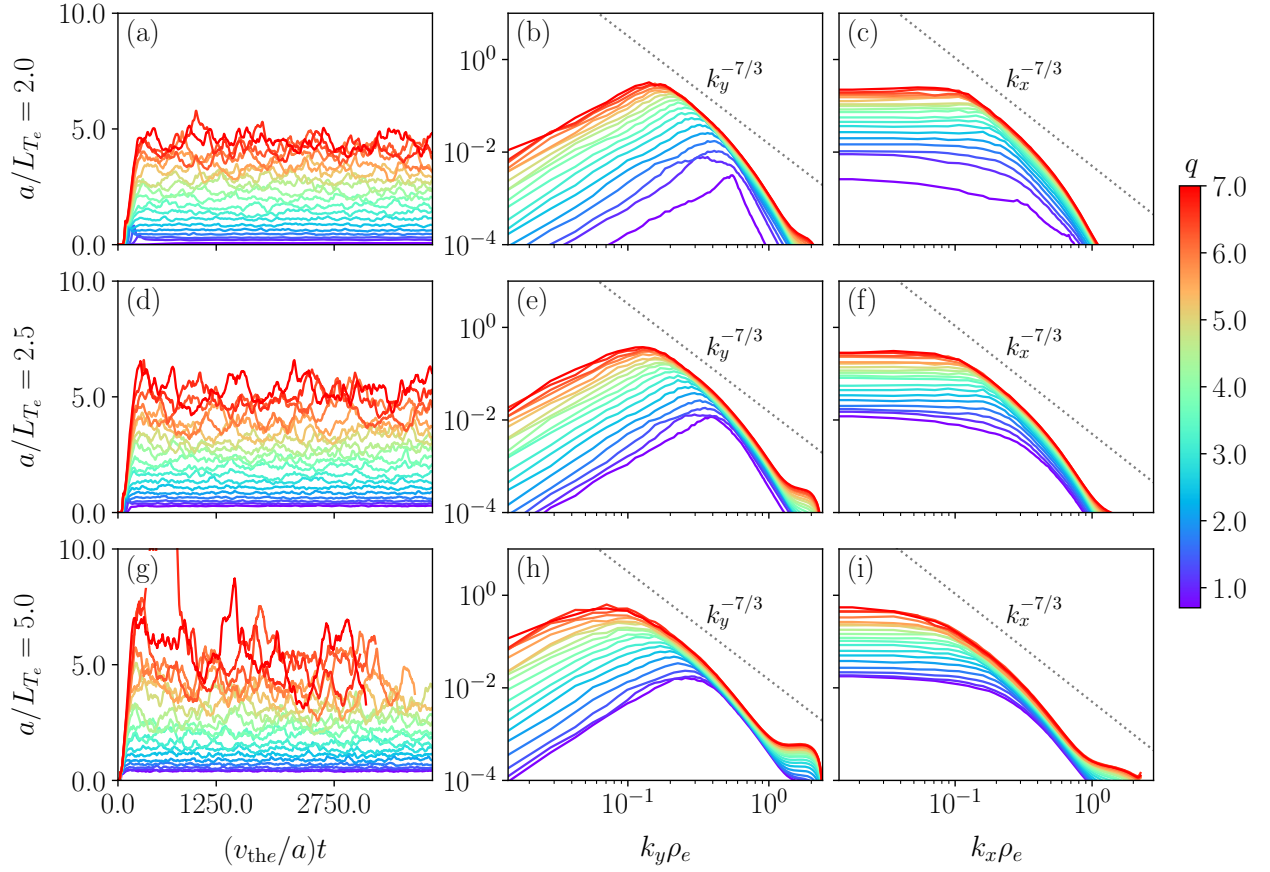


FIG. 14. Data from the simulations labelled ‘CBC ETG  $q$ ’ in table I, with each row corresponding to a different value of  $a/L_{T_e}$ . The colours indicate the value of  $q$  for a given simulation, where all data shown is normalised to  $Q_{\text{gBe}} = n_e T_e v_{\text{the}} (\rho_e/a)^2$  and rescaled by  $(a/L_{T_e})^3$  [see (24)]. First column: heat fluxes as functions of time. Second column: time-averaged one-dimensional binormal heat-flux spectra (22). Third column: time-averaged one-dimensional radial heat-flux spectra (23).

- [17] S. C. Cowley, R. M. Kulsrud, and R. Sudan, Considerations of ion-temperature-gradient-driven turbulence, *Phys. Fluids B* **3**, 2767 (1991).
- [18] M. Kotschenreuther, W. Dorland, M. A. Beer, and G. W. Hammett, Quantitative predictions of tokamak energy confinement from first-principles simulations with kinetic effects, *Phys. Plasmas* **2**, 2381 (1995).
- [19] C. M. Roach, D. J. Applegate, J. W. Connor, S. C. Cowley, W. D. Dorland, R. J. Hastie, N. Joiner, S. Saarelma, A. A. Schekochihin, R. J. Akers, C. Brickley, A. R. Field, M. Valovic, and MAST Team, Microstability physics as illuminated in the spherical tokamak, *Plasma Phys. Control. Fusion* **47**, B323 (2005).
- [20] C. M. Roach, I. G. Abel, R. J. Akers, W. Arter, M. Barnes, Y. Camenen, F. J. Casson, G. Colyer, J. W. Connor, S. C. Cowley, D. Dickinson, W. Dorland, A. R. Field, W. Guttenfelder, G. W. Hammett, R. J. Hastie, E. Highcock, N. F. Loureiro, A. G. Peeters, M. Reshko, S. Saarelma, A. A. Schekochihin, M. Valovic, and H. R. Wilson, Gyrokinetic simulations of spherical tokamaks, *Plasma Phys. Control. Fusion* **51**, 124020 (2009).
- [21] W. Guttenfelder, J. L. Peterson, J. Candy, S. M. Kaye, Y. Ren, R. E. Bell, G. W. Hammett, B. P. LeBlanc, D. R. Mikkelsen, W. M. Nevins, and H. Yuh, Progress in simulating turbulent electron thermal transport in NSTX, *Nucl. Fusion* **53**, 093022 (2013).
- [22] W. Guttenfelder, R. J. Groebner, J. M. Canik, B. A. Grierson, E. A. Belli, and J. Candy, Testing predictions of electron scale turbulent pedestal transport in two DIII-D ELMy H-modes, *Nucl. Fusion* **61**, 056005 (2021).
- [23] Y. Ren, E. Belova, N. Gorelenkov, W. Guttenfelder, S. M. Kaye, E. Mazzucato, J. L. Peterson, D. R. Smith, D. Stutman, K. Tritz, W. X. Wang, H. Yuh, R. E. Bell, C. W. Domier, and B. P. LeBlanc, Recent progress in understanding electron thermal transport in NSTX, *Nucl. Fusion* **57**, 072002 (2017).
- [24] M. Barnes, F. I. Parra, and A. A. Schekochihin, Critically balanced ion temperature gradient turbulence in fusion plasmas, *Phys. Rev. Lett.* **107**, 115003 (2011).
- [25] T. Adkins, A. A. Schekochihin, P. G. Ivanov, and C. M. Roach, Electromagnetic instabilities and plasma turbulence driven by electron-temperature gradient, *J. Plasma Phys.* **88**, 905880410 (2022).
- [26] R. Nies, F. I. Parra, M. Barnes, N. Mandell, and W. Dorland, Saturation of magnetised plasma turbulence by propagating zonal flows, arXiv e-prints **arXiv:2409.02283** (2024).

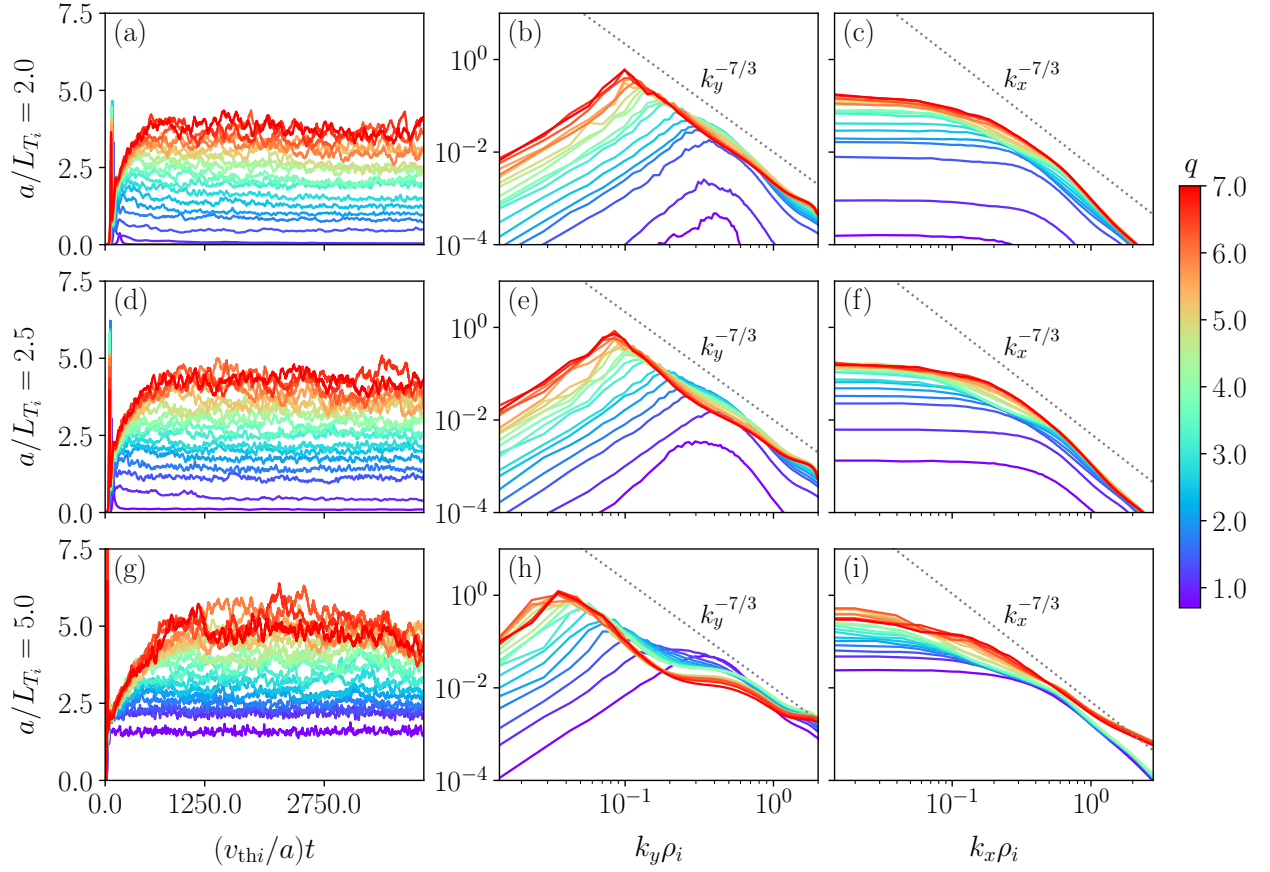


FIG. 15. Data from the simulations labelled ‘CBC ITG  $q$ ’ in table I, with each row corresponding to a different value of  $a/L_{T_i}$ . The colours indicate the value of  $q$  for a given simulation, and all data shown is normalised to  $Q_{\text{gBi}} = n_i T_i v_{\text{thi}} (\rho_i/a)^2$  and rescaled by  $(a/L_{T_i})^1$  [see (26)]. First column: heat fluxes as functions of time. Second column: time-averaged one-dimensional binormal heat-flux spectra (22). Third column: time-averaged one-dimensional radial heat-flux spectra (23).

- [27] Y.-c. Ghim, A. A. Schekochihin, A. R. Field, I. G. Abel, M. Barnes, G. Colyer, S. C. Cowley, F. I. Parra, D. Dunai, and S. Zoleznik, Experimental signatures of critically balanced turbulence in MAST, *Phys. Rev. Lett.* **110**, 145002 (2013).
- [28] R. C. Wolf, Internal transport barriers in tokamak plasmas, *Plasma Phys. Control. Fusion* **45**, R1 (2003).
- [29] T. G. Adkins, Electromagnetic instabilities and plasma turbulence driven by the electron-temperature gradient, Ph.D. thesis, University of Oxford (URL: <https://ora.ox.ac.uk/objects/uuid:337d61a1-7997-435c-975e-4928cc3902ea>) (2023).
- [30] T. Adkins, P. G. Ivanov, and A. A. Schekochihin, Scale invariance and critical balance in electrostatic drift-kinetic turbulence, *J. Plasma Phys.* **89**, 905890406 (2023).
- [31] P. G. Ivanov, T. Adkins, D. Kennedy, M. Giacomin, M. Barnes, and A. A. Schekochihin, Suppression of temperature-gradient-driven turbulence by sheared flows in fusion plasmas, *J. Plasma Phys.* **91**, e58 (2025).
- [32] M. A. Beer, S. C. Cowley, and G. W. Hammett, Field-aligned coordinates for nonlinear simulations of tokamak turbulence, *Phys. Plasmas* **2**, 2687 (1995).
- [33] P. G. Ivanov, P. Luhadiya, T. Adkins, and A. A. Schekochihin, The gyrokinetic field invariant and electromagnetic temperature-gradient instabilities in ‘good-curvature’ plasmas, *J. Plasma Phys.* **91**, E95 (2025).
- [34] A. A. Schekochihin, S. C. Cowley, W. Dorland, G. W. Hammett, G. G. Howes, E. Quataert, and T. Tatsuno, Astrophysical gyrokinetics: kinetic and fluid turbulent cascades in magnetized weakly collisional plasmas, *Astrophys. J. Suppl.* **182**, 310 (2009).
- [35] P. A. Davidson, Turbulence in Rotating, Stratified and Electrically Conducting Fluids (Cambridge University Press, Cambridge, 2013).
- [36] A. B. Hassam, J. Antonsen, T. M., J. F. Drake, and P. N. Guzdar, Theory of ion temperature gradient instabilities: Thresholds and transport, *Phys. Fluids B* **2**, 1822 (1990).
- [37] S. C. Guo and F. Romanelli, The linear threshold of the ion-temperature-gradient-driven mode, *Phys. Fluids B* **5**, 520 (1993).
- [38] A. I. Smolyakov, M. Yagi, and Y. Kishimoto, Short wavelength temperature gradient driven modes in tokamak plasmas, *Phys. Rev. Lett.* **89**, 125005 (2002).

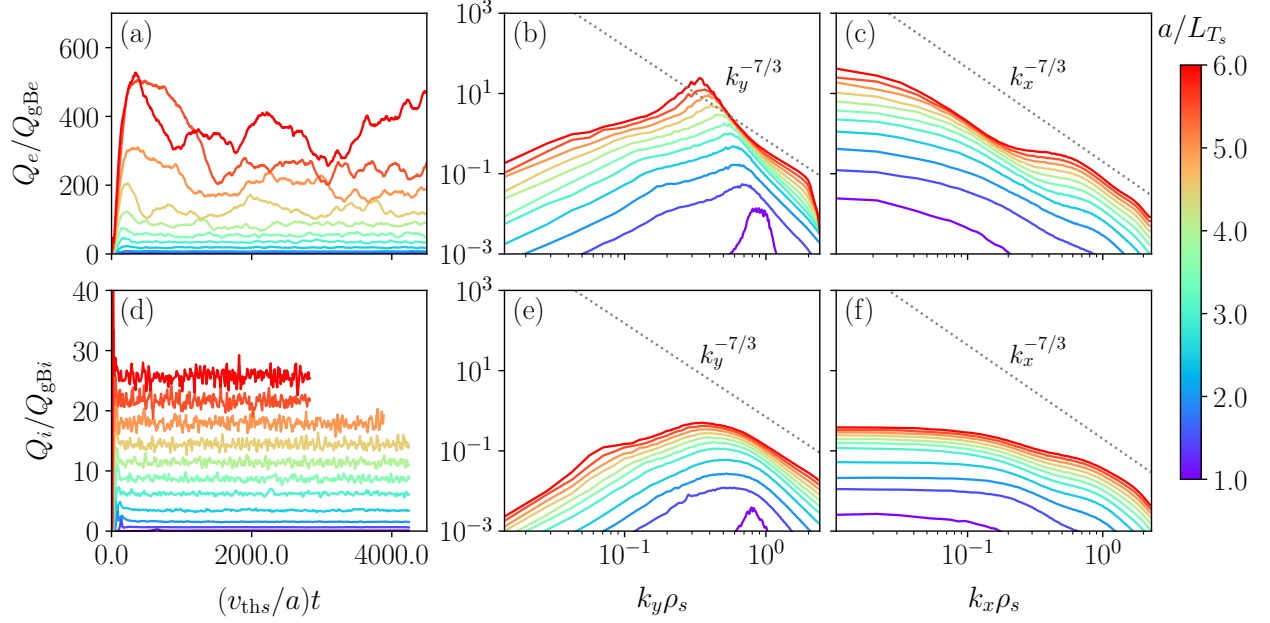


FIG. 16. Data from the simulations labelled ‘NCSX ETG  $L_{T_e}$ ’ and ‘NCSX ITG  $L_{T_i}$ ’ in table I, shown in the top and bottom rows, respectively. The colours indicate the value of  $a/L_{T_s}$  for the given simulation, and all data shown is normalised to  $Q_{gBs} = n_s T_s v_{th}s (\rho_s/a)^2$ . First column: heat fluxes as functions of time. Second column: time-averaged one-dimensional binormal heat-flux spectra (22). Third column: time-averaged one-dimensional radial heat-flux spectra (23).

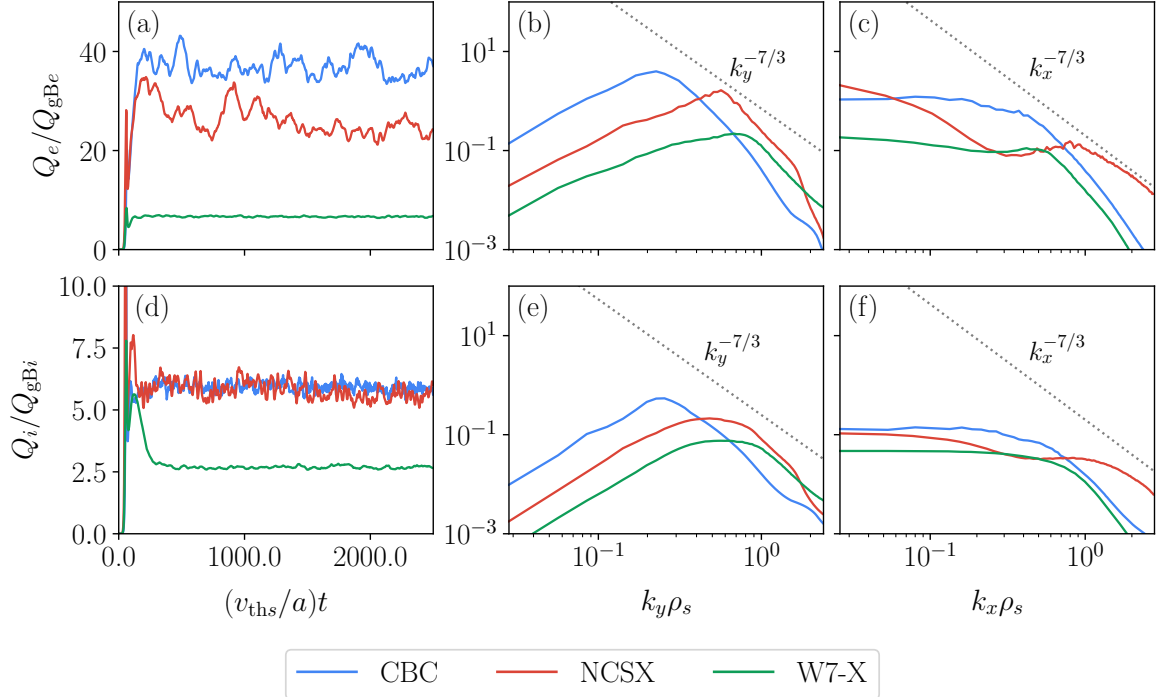


FIG. 17. Data from the simulations labelled ‘CBC ETG  $L_{\parallel}$ ’, ‘CBC ITG  $L_{\parallel}$ ’, ‘NCSX ETG  $L_{\parallel}$ ’, ‘NCSX ITG  $L_{\parallel}$ ’, ‘W7-X ETG  $L_{\parallel}$ ’, and ‘W7-X ITG  $L_{\parallel}$ ’ in table I. The colours indicate different magnetic equilibria, and all data shown is normalised to  $Q_{gBs} = n_s T_s v_{th}s (\rho_s/a)^2$ . First column: heat fluxes as functions of time. Second column: time-averaged one-dimensional binormal heat-flux spectra (22). Third column: time-averaged one-dimensional radial heat-flux spectra (23).

[39] O. Gupta, M. Barnes, F. I. Parra, L. Podavini, A. Zocco, T. Adkins, and P. G. Ivanov, Scaling laws for the cutoff wavenumber of the short-wavelength, ion-temperature-gradient mode in a z-pinch (2025), in preparation for *J. Plasma Phys.*

[40] A. A. Schekochihin, J. T. Parker, E. G. Highcock, P. J. Dellar, W. Dorland, and G. W. Hammett, Phase mixing versus nonlinear advection in drift-kinetic plasma turbulence, *J. Plasma Phys.* **82**, 905820212 (2016).

[41] P. Goldreich and S. Sridhar, Toward a theory of interstellar turbulence. 2: Strong Alfvénic turbulence, *Astrophys. J.* **438**, 763 (1995).

[42] S. Boldyrev, On the spectrum of magnetohydrodynamic turbulence, *Astrophys. J.* **626**, L37 (2005).

[43] A. A. Schekochihin, MHD turbulence: a biased review, *J. Plasma Phys.* **88**, 155880501 (2022).

[44] W. Dorland and G. W. Hammett, Gyrofluid turbulence models with kinetic effects, *Phys. Fluids B* **5**, 812 (1993).

[45] G. W. Hammett, M. A. Beer, W. Dorland, S. C. Cowley, and S. A. Smith, Developments in the gyrofluid approach to tokamak turbulence simulations, *Plasma Phys. Control. Fusion* **35**, 973 (1993).

[46] I. G. Abel and S. C. Cowley, Multiscale gyrokinetics for rotating tokamak plasmas: II. Reduced models for electron dynamics, *New J. Phys.* **15**, 023041 (2013).

[47] B. N. Rogers, W. Dorland, and M. Kotschenreuther, Generation and stability of zonal flows in ion-temperature-gradient mode turbulence, *Phys. Rev. Lett.* **85**, 5336 (2000).

[48] B. N. Rogers, W. Dorland, and M. Kotschenreuther, Noncurvature-driven modes in a transport barrier, *Phys. Plasmas* **12**, 062511 (2005).

[49] P. G. Ivanov, A. A. Schekochihin, W. Dorland, A. R. Field, and F. I. Parra, Zonally dominated dynamics and Dimits threshold in curvature-driven ITG turbulence, *J. Plasma Phys.* **86**, 855860502 (2020).

[50] A. M. Dimits, G. Bateman, M. A. Beer, B. I. Cohen, W. Dorland, G. W. Hammett, C. Kim, J. E. Kinsey, M. Kotschenreuther, A. H. Kritz, L. L. Lao, J. Mandrekas, W. M. Nevins, S. E. Parker, A. J. Redd, D. E. Shumaker, R. Sydora, and J. Weiland, Comparisons and physics basis of tokamak transport models and turbulence simulations, *Phys. Plasmas* **7**, 969 (2000).

[51] P. G. Ivanov, A. A. Schekochihin, and W. Dorland, Dimits transition in three-dimensional ion-temperature-gradient turbulence, *J. Plasma Phys.* **88**, 905880506 (2022).

[52] V. N. Faddeeva and N. M. Terent'ev, Tables of Values of the Function  $w(z) = \exp(-z^2)(1 + 2i/\sqrt{\pi} \int_0^z \exp(t^2) dt)$  for Complex Argument (Moscow: Gostekhizdat, English translation: New York: Pergamon Press, 1961, 1954).

[53] B. D. Fried and S. D. Conte, The Plasma Dispersion Function (Academic Press, New York, 1961).

[54] M. Abramowitz and I. A. Stegun, Handbook of Mathematical Functions (1972).

[55] D. N. Hosking and A. A. Schekochihin, Emergence of long-range correlations and thermal spectra in forced turbulence, arXiv e-prints **2202.00462** (2022).

[56] M. D. Kruskal and R. M. Kulsrud, Equilibrium of a Magnetically Confined Plasma in a Toroid, *Physics of Fluids* **1**, 265 (1958).

[57] W. D. D'Haeseleer, W. N. G. Hitchon, J. D. Callen, and J. L. Shohet, Flux Coordinates and Magnetic Field Structure (Springer Berlin, Heidelberg, 1991).

[58] J. F. Parisi, F. I. Parra, C. M. Roach, C. Giroud, W. Dorland, D. R. Hatch, M. Barnes, J. C. Hillesheim, N. Aiba, J. Ball, P. G. Ivanov, and J. contributors, Toroidal and slab ETG instability dominance in the linear spectrum of JET-ILW pedestals, *Nucl. Fusion* **60**, 126045 (2020).

[59] J. F. Parisi, F. I. Parra, C. M. Roach, M. R. Hardman, A. A. Schekochihin, I. G. Abel, N. Aiba, J. Ball, M. Barnes, B. Chapman-Olopouli, D. Dickinson, W. Dorland, C. Giroud, D. R. Hatch, J. C. Hillesheim, J. Ruiz Ruiz, S. Saarelma, D. St-Onge, and J. Contributors, Three-dimensional inhomogeneity of electron-temperature-gradient turbulence in the edge of tokamak plasmas, *Nucl. Fusion* **62**, 086045 (2022).

[60] G. J. Colyer, A. A. Schekochihin, F. I. Parra, C. M. Roach, M. A. Barnes, Y.-c. Ghim, and W. Dorland, Collisionality scaling of the electron heat flux in ETG turbulence, *Plasma Phys. Control. Fusion* **59**, 055002 (2017).

[61] S. Tirkas, G. Chen, H. an Merlo, F. Jenko, and P. Parker, Zonal flow excitation in electron-scale tokamak turbulence, *Nucl. Fusion* **63**, 026015 (2023).

[62] R. Nies and F. I. Parra, Theory of zonal flow growth and propagation in toroidal geometry, arXiv e-prints **arXiv:2504.09785** (2025).

[63] E. Kim and P. H. Diamond, Dynamics of zonal flow saturation in strong collisionless drift wave turbulence, *Phys. Plasmas* **9**, 4530 (2002).

[64] P. H. Diamond, S.-I. Itoh, K. Itoh, and T. S. Hahm, Zonal flows in plasma—a review, *Plasma Phys. Control. Fusion* **47** (2005).

[65] S. Kobayashi and B. Rogers, The quench rule, Dimits shift, and eigenmode localization by small-scale zonal flows, *Phys. Plasmas* **19**, 012315 (2012).

[66] L. Villard, P. Angelino, A. Bottino, S. Brunner, S. Jolliet, B. F. McMillan, T. M. Tran, and T. Vernay, Global gyrokinetic ion temperature gradient turbulence simulations of ITER, *Plasma Phys. Control. Fusion* **55**, 074017 (2013).

[67] L. Villard, B. F. McMillan, O. Sauter, F. Hariri, J. Dominski, G. Merlo, S. Brunner, and T. M. Tran, Turbulence and zonal flow structures in the core and L-mode pedestal of tokamak plasmas, *J. Phys. Conf. Ser.* **561**, 012022 (2014).

[68] H. Zhu, Y. Zhou, and I. Y. Dodin, Theory of the Tertiary Instability and the Dimits Shift from Reduced Drift-Wave Models, *Phys. Rev. Lett.* **124**, 055002 (2020).

[69] Z. Lin, T. S. Hahm, W. W. Lee, W. M. Tang, and P. H. Diamond, Effects of Collisional Zonal Flow Damping on Turbulent Transport, *Phys. Rev. Lett.* **83**, 3645 (1999).

[70] B. Chapman-Oplopoio, D. R. Hatch, A. R. Field, L. Frassinetti, J. Hillesheim, L. Horvath, C. F. Maggi, J. Parisi, C. M. Roach, S. Saarelma, and J. Walker, The role of ETG modes in JET-ILW pedestals with varying levels of power and fuelling, *Nucl. Fusion* **62**, 086028 (2022).

[71] G. G. Plunk, P. Helander, P. Xanthopoulos, and J. W. Connor, Collisionless microinstabilities in stellarators. III. The ion-temperature-gradient mode, *Phys. Plasmas* **21**, 032112 (2014).

[72] M. C. Zarnstorff, L. A. Berry, A. Brooks, E. Fredrickson, G.-Y. Fu, S. Hirshman, S. Hudson, L.-P. Ku, E. Lazarus, D. Mikkelsen, D. Monticello, G. H. Neilson, N. Pomphrey, A. Reiman, D. Spong, D. Strickler, A. Boozer, W. A. Cooper, R. Goldston, R. Hatcher, M. Isaev, C. Kessel, J. Lewandowski, J. F. Lyon, P. Merkel, H. Mynick, B. E. Nelson, C. Nuehrenberg, M. Redi, W. Reiersen, P. Rutherford, R. Sanchez, J. Schmidt, and R. B. White, Physics of the compact advanced stellarator NCSX, *Plasma Phys. Control. Fusion* **43**, 237 (2001).

[73] J. Geiger, C. D. Beidler, Y. Feng, H. Maaßberg, N. B. Marushchenko, and Y. Turkin, Physics in the magnetic configuration space of W7-X, *Plasma Phys. Control. Fusion* **57**, 014004 (2014).

[74] G. T. Roberg-Clark, G. G. Plunk, and P. Xanthopoulos, Coarse-grained gyrokinetics for the critical ion temperature gradient in stellarators, *Phys. Rev. Res.* **4**, L032028 (2022).

[75] E. Rodríguez and A. Zocco, The kinetic ion-temperature-gradient-driven instability and its localisation, *J. Plasma Phys.* **91**, E21 (2025).

[76] A. G. Goodman, P. Xanthopoulos, G. G. Plunk, H. Smith, C. Nührenberg, C. D. Beidler, S. A. Henneberg, G. Roberg-Clark, M. Drevlak, and P. Helander, Quasi-isodynamic stellarators with low turbulence as fusion reactor candidates, *Phys. Rev. X Energy* **3**, 023010 (2024).

[77] P. Kim, S. Buller, R. Conlin, W. Dorland, D. W. Dutt, R. Gaur, R. Jorge, E. Kolemen, M. Landreman, N. R. Mandell, and D. Panici, Optimization of nonlinear turbulence in stellarators, *J. Plasma Phys.* **90**, 905900210 (2024).

[78] M. Landreman, J. Y. Choi, C. Alves, P. Balaprakash, M. Churchill, R. Conlin, and G. Roberg-Clark, How does ion temperature gradient turbulence depend on magnetic geometry? Insights from data and machine learning, *J. Plasma Phys.* **91**, E120 (2025).

[79] H. Thienpondt, J. M. García-Regaña, I. Calvo, G. Acton, and M. Barnes, Influence of the density gradient on turbulent heat transport at ion-scales: an inter-machine study with the gyrokinetic code stella, *Nucl. Fusion* **65**, 016062 (2025).

[80] P. Helander, A. Mishchenko, R. Kleiber, and P. Xanthopoulos, Oscillations of zonal flows in stellarators, *Plasma Phys. Control. Fusion* **53**, 054006 (2011).

[81] J. A. Alonso, E. Sánchez, I. Calvo, J. L. Velasco, K. J. McCarthy, A. Chmyga, L. G. Eliseev, T. Estrada, R. Kleiber, L. I. Krupnik, A. V. Melnikov, P. Monreal, F. I. Parra, S. Perfilov, A. I. Zhezhera, and the TJ-II Team, Observation of Oscillatory Radial Electric Field Relaxation in a Helical Plasma, *Phys. Rev. Lett.* **118**, 185002 (2017).

[82] E. Sánchez, A. Mishchenko, J. M. García-Regaña, R. Kleiber, A. Bottino, L. Villard, and the W7-X Team, Nonlinear gyrokinetic PIC simulations in stellarators with the code EUTERPE, *J. Plasma Phys.* **86**, 855860501 (2020).

[83] G. O. Acton, Modelling and optimising turbulence in 3D magnetic geometries for enhanced microstability, Ph.D. thesis, University of Oxford (URL: <https://ora.ox.ac.uk/objects/uuid:78daaa1f-6954-4e00-b801-0882691e5997>) (2025).

[84] A. R. Field, B. Chapman-Oplopoio, J. W. Connor, L. Frassinetti, D. R. Hatch, C. M. Roach, S. Saarelma, and JET contributors, Comparing pedestal structure in JET-ILW h-mode plasmas with a model for stiff etg turbulent heat transport, *Philos. Trans. R. Soc. London A* **381**, 20210228 (2023).

[85] L.-P. Turica, A. R. Field, L. Frassinetti, A. A. Schekochihin, J. Contributors, and the EUROfusion Tokamak Exploitation Team, Reconstructions of electron-temperature profiles from EUROfusion Pedestal Database using turbulence models and machine learning, arXiv e-prints [arXiv:2504.17486](https://arxiv.org/abs/2504.17486) (2025).

[86] Y. Shimomura, Y. Murakami, A. R. Polevoi, P. Barabaschi, V. Mukhovatov, and M. Shimada, ITER: opportunity of burning plasma studies, *Plasma Phys. Control. Fusion* **43**, 385 (2001).

[87] A. C. C. Sips, Advanced scenarios for ITER operation, *Plasma Phys. Control. Fusion* **47**, A19 (2005).

[88] C. C. Hegna, D. T. Anderson, E. C. Andrew, A. Ayilaran, A. Bader, T. D. Bohm, K. Camacho Mata, J. M. Canik, L. Carbalal, A. Cerfon, *et al.*, The Infinity Two fusion pilot plant baseline plasma physics design, *J. Plasma Phys.* **91**, E76 (2025).

[89] J. Lion, J.-C. Anglès, L. Bonauer, A. Bañón Navarro, S. A. Cadena Ceron, R. Davies, M. Drevlak, N. Foppiani, J. Geiger, A. Goodman, W. Guo, E. Guiraud, F. Hernández, S. Henneberg, R. Herrero, C. Hintze, H. Höchter, J. Jelonnek, F. Jenko, R. Jorge, M. Kaiser, M. Kubie, E. Lascas Neto, H. Laqua, M. Leoni, J. F. Lobsien, V. Maurin, A. Merlo, D. Middleton-Gear, M. Pascu, G. G. Plunk, N. Riva, M. Savtchouk, F. Sciortino, J. Schilling, J. Shimwell, A. Di Siena, R. Slade, T. Stange, T. N. Todd, L. Wegener, F. Wilms, P. Xanthopoulos, and M. Zheng, Stellaris: A high-field quasi-isodynamic stellarator for a prototypical fusion power plant, *Fus. Eng. Des.* **214**, 114868 (2025).

[90] G. G. Plunk, P. Xanthopoulos, G. M. Weir, S. A. Bozhenkov, A. Dinklage, G. Fuchert, J. Geiger, M. Hirsch, U. Hoefel, M. Jakubowski, A. Langenberg, N. Pablant, E. Pasch, T. Stange, D. Zhang, and the W7-X Team, Stellarators Resist Turbulent Transport on the Electron Larmor Scale, *Phys. Rev. Lett.* **122**, 035002 (2019).

[91] P. Xanthopoulos, S. A. Bozhenkov, M. N. Beurskens, H. M. Smith, G. G. Plunk, P. Helander, C. D. Beidler, J. A. Alcúson, A. Alonso, A. Dinklage, O. Ford, G. Fuchert, J. Geiger, J. H. E. Proll, M. J. Pueschel, Y. Turkin, F. Warmer, and the W7-X Team, Turbulence Mechanisms of Enhanced Performance Stellarator Plasmas, *Phys. Rev. Lett.* **125**, 075001 (2020).

[92] G. M. Weir, P. Xanthopoulos, M. Hirsch, U. Höfel, T. Stange, N. Pablant, O. Grulke, S. Åkäslompolo, J. Alcúson, S. Bozhenkov, M. Beurskens, A. Dinklage, G. Fuchert, J. Geiger, M. Landreman, A. Langenberg, S. Lazerson, N. Marushchenko, E. Pasch, J. Schilling, E. R. Scott, Y. Turkin, T. Klinger, and the W7-X Team, Heat pulse propagation and anomalous electron heat transport measurements on the optimized stellarator W7-X, *Nucl. Fusion* **61**, 056001 (2021).

[93] F. Wilms, A. Bañón Navarro, T. Windisch, S. Bozhenkov, F. Warmer, G. Fuchert, O. Ford, D. Zhang, T. Stange, F. Jenko, and the W7-X Team, Global gyrokinetic analysis of Wendelstein 7-X discharge: unveiling the importance of trapped-electron-mode and electron-temperature-gradient turbulence, *Nucl. Fusion* **64**, 096040 (2024).

[94] D. A. St-Onge, On non-local energy transfer via zonal flow in the Dimits shift, *J. Plasma Phys.* **83**, 905830504 (2017).

[95] H. Zhu, Y. Zhou, and I. Y. Dodin, Theory of the tertiary instability and the Dimits shift within a scalar model, *J. Plasma Phys.* **86**, 905860405 (2020).

[96] D. R. Hatch, C. Michoski, D. Kuang, B. Chapman-Oplopoioi, M. Curie, M. Halfmoon, E. Hassan, M. Kotschenreuther, S. M. Mahajan, G. Merlo, M. J. Pueschel, J. Walker, and C. D. Stephens, Reduced models for ETG transport in the tokamak pedestal, *Phys. Plasmas* **29**, 062501 (2022).

[97] X. Garbet, P. Mantica, C. Angioni, E. Asp, Y. Baranov, C. Bourdelle, R. Budny, F. Crisanti, G. Cordey, L. Garzotti, N. Kirneva, D. Hogeweij, T. Hoang, F. Imbeaux, E. Joffrin, X. Litaudon, A. Manini, D. C. McDonald, H. Nordman, V. Parail, A. Peeters, F. Ryter, C. Sozzi, M. Valovic, T. Tala, A. Thyagaraja, I. Voitsekhovitch, J. Weiland, H. Weisen, A. Zabolotsky, and the JET EFDA Contributors, Physics of transport in tokamaks, *Plasma Phys. Control. Fusion* **46**, B557 (2004).

[98] P. Mantica, D. Strintzi, T. Tala, C. Giroud, T. Johnson, H. Leggate, E. Lerche, T. Loarer, A. G. Peeters, A. Salmi, S. Sharapov, D. Van Eester, P. C. de Vries, L. Zabeo, and K.-D. Zastrow, Experimental Study of the Ion Critical-Gradient Length and Stiffness Level and the Impact of Rotation in the JET Tokamak, *Phys. Rev. Lett.* **102**, 175002 (2009).

[99] J. C. Adam, G. Laval, and R. Pellat, Localized drift dissipative modes in Tokamaks, *Nucl. Fusion* **13**, 47 (1973).

[100] J. C. Adam, W. M. Tang, and P. H. Rutherford, Destabilization of the trapped-electron mode by magnetic curvature drift resonances, *Phys. Fluids* **19**, 561 (1976).

[101] P. J. Catto, Linearized gyro-kinetics, *Plasma Physics* **20**, 719 (1978).

[102] C. Z. Cheng and L. Chen, Ballooning-mode theory of trapped-electron instabilities in tokamaks, *Nucl. Fusion* **21**, 403 (1981).

[103] J. H. E. Proll, P. Helander, J. W. Connor, and G. G. Plunk, Resilience of Quasi-Isodynamic Stellarators against Trapped-Particle Instabilities, *Phys. Rev. Lett.* **108**, 245002 (2012).

[104] P. Helander, J. H. E. Proll, and G. G. Plunk, Collisionless microininstabilities in stellarators. I. Analytical theory of trapped-particle modes, *Phys. Plasmas* **20**, 122505 (2013).

[105] E. Rodríguez, P. Helander, and A. G. Goodman, The maximum-J property in quasi-isodynamic stellarators, *J. Plasma Phys.* **90**, 905900212 (2024).

[106] J. Candy, R. E. Waltz, M. R. Fahey, and C. Holland, The effect of ion-scale dynamics on electron-temperature-gradient turbulence, *Plasma Phys. Control. Fusion* **49**, 1209 (2007).

[107] R. E. Waltz, J. Candy, and M. Fahey, Coupled ion temperature gradient and trapped electron mode to electron temperature gradient mode gyrokinetic simulations, *Phys. Plasmas* **14**, 056116 (2007).

[108] S. Maeyama, Y. Idomura, T. H. Watanabe, M. Nakata, M. Yagi, N. Miyato, A. Ishizawa, and M. Nunami, Cross-Scale Interactions between Electron and Ion Scale Turbulence in a Tokamak Plasma, *Phys. Rev. Lett.* **114**, 255002 (2015).

[109] N. T. Howard, C. Holland, A. E. White, M. Greenwald, and J. Candy, Multi-scale gyrokinetic simulation of tokamak plasmas: enhanced heat loss due to cross-scale coupling of plasma turbulence, *Nuclear Fusion* **56**, 014004 (2016).

[110] N. T. Howard, C. Holland, A. E. White, M. Greenwald, J. Candy, and A. J. Creely, Multi-scale gyrokinetic simulations: Comparison with experiment and implications for predicting turbulence and transport, *Physics of Plasmas* **23**, 056109 (2016).

[111] M. R. Hardman, M. Barnes, and C. M. Roach, Stabilisation of short-wavelength instabilities by parallel-to-the-field shear in long-wavelength ExB flows, *J. Plasma Phys.* **86**, 905860601 (2020).

[112] J. F. Drake and Y. C. Lee, Kinetic theory of tearing instabilities, *Phys. Fluids* **20**, 1341 (1977).

[113] J. F. Drake, N. T. Gladd, C. S. Liu, and C. L. Chang, Microtearing modes and anomalous transport in tokamaks, *Phys. Rev. Lett.* **44**, 994 (1980).

[114] A. B. Hassam, Fluid theory of tearing instabilities, *Phys. Fluids* **23**, 2493 (1980).

[115] A. B. Hassam, Higher-order Chapman-Enskog theory for electrons, *Phys. Fluids* **23**, 38 (1980).

[116] A. Zocco, N. F. Loureiro, D. Dickinson, R. Numata, and C. M. Roach, Kinetic microtearing modes and reconnecting modes in strongly magnetised slab plasmas, *Plasma Phys. Control. Fusion* **57**, 065008 (2015).

[117] J. L. Larakers, R. D. Hazeltine, and S. M. Mahajan, A comprehensive conductivity model for drift and micro-tearing modes, *Phys. Plasmas* **27**, 062503 (2020).

[118] J. L. Larakers, M. Curie, D. R. Hatch, R. D. Hazeltine, and S. M. Mahajan, Global theory of microtearing modes in the tokamak pedestal, *Phys. Rev. Lett.* **126**, 225001 (2021).

[119] B. D. G. Chandran and A. A. Schekochihin, A gyrokinetic dispersion relation for microtearing modes in toroidal plasmas with cold ions, *J. Plasma Phys.* **90**, 10.1017/S0022377824000175 (2024).

[120] M. R. Hardman, F. I. Parra, B. S. Patel, C. M. Roach, J. Ruiz Ruiz, M. Barnes, D. Dickinson, W. Dorland, J. F. Parisi, D. St-Onge, and H. Wilson, New linear stability parameter to describe low- $\beta$  electromagnetic microininstabilities driven by passing electrons in axisymmetric toroidal geometry, *Plasma Phys. Control. Fusion* **65**, 045011 (2023).

[121] B. Patel, M. R. Hardman, D. Kennedy, M. Giacomin, D. Dickinson, and C. M. Roach, The impact of  $\mathbf{E} \times \mathbf{B}$  shear on microtearing-based transport in spherical tokamaks, *Nucl. Fusion* **65**, 026063 (2025).

[122] W. M. Tang, J. W. Connor, and R. J. Hastie, Kinetic-ballooning-mode theory in general geometry, *Nucl. Fusion* **20**, 1439 (1980).

[123] P. B. Snyder, *Gyrofluid theory and simulation of electromagnetic turbulence and transport in tokamak plasmas*, Ph.D. thesis, Princeton University (URL: <https://w3.ppp1.gov/~hammett/gyrofluid/papers/1999/thesis.pdf>) (1999).

[124] P. B. Snyder and G. W. Hammett, Electromagnetic effects on plasma microturbulence and transport, *Phys. Plasmas* **8**, 744 (2001).

[125] P. B. Snyder and G. W. Hammett, A Landau fluid model for electromagnetic plasma microturbulence, *Phys. Plasmas* **8**, 3199 (2001).

[126] M. J. Pueschel, M. Kammerer, and F. Jenko, Gyrokinetic turbulence simulations at high plasma beta, *Phys. Plasmas* **15**, 102310 (2008).

[127] M. J. Pueschel and F. Jenko, Transport properties of finite- $\beta$  microturbulence, *Phys. Plasmas* **17**, 062307 (2010).

[128] R. E. Waltz, Nonlinear subcritical magnetohydrodynamic beta limit, *Phys. Plasmas* **17**, 072501 (2010).

[129] W. Wan, S. E. Parker, Y. Chen, Z. Yan, R. J. Groebner, and P. B. Snyder, Global Gyrokinetic Simulation of Tokamak Edge Pedestal Instabilities, *Phys. Rev. Lett.* **109**, 185004 (2012).

[130] W. Wan, S. E. Parker, Y. Chen, R. J. Groebner, Z. Yan, A. Y. Pankin, and S. E. Kruger, Global gyrokinetic simulations of the h-mode tokamak edge pedestal, *Phys. Plasmas* **20**, 055902 (2013).

[131] A. Ishizawa, S. Maeyama, T. H. Watanabe, H. Sugama, and N. Nakajima, Gyrokinetic turbulence simulations of high-beta tokamak and helical plasmas with full-kinetic and hybrid models, *Nucl. Fusion* **53**, 053007 (2013).

[132] A. Ishizawa, T.-H. Watanabe, H. Sugama, S. Maeyama, and N. Nakajima, Electromagnetic gyrokinetic turbulence in finite-beta helical plasmas, *Phys. Plasmas* **21**, 055905 (2014).

[133] A. Ishizawa, D. Urano, Y. Nakamura, S. Maeyama, and T. H. Watanabe, Persistence of Ion Temperature Gradient Turbulent Transport at Finite Normalized Pressure, *Phys. Rev. Lett.* **123**, 025003 (2019).

[134] P. W. Terry, D. Carmody, H. Doerk, W. Guttenfelder, D. R. Hatch, C. C. Hegna, A. Ishizawa, F. Jenko, W. M. Nevins, I. Predebon, M. J. Pueschel, J. S. Sarff, and G. G. Whelan, Overview of gyrokinetic studies of finite-beta microturbulence, *Nucl. Fusion* **55**, 104011 (2015).

[135] K. Aleynikova and A. Zocco, Quantitative study of kinetic ballooning mode theory in simple geometry, *Phys. Plasmas* **24**, 092106 (2017).

[136] D. Kennedy, M. Giacomin, F. J. Casson, D. Dickinson, W. A. Hornsby, B. S. Patel, and C. M. Roach, Electromagnetic gyrokinetic instabilities in STEP, *Nucl. Fusion* **63**, 126061 (2023).

[137] D. Kennedy, C. M. Roach, M. Giacomin, P. G. Ivanov, T. Adkins, F. Sheffield, T. Görler, A. Bokshi, D. Dickinson, H. G. Dudding, and B. S. Patel, On the importance of parallel magnetic-field fluctuations for electromagnetic instabilities in STEP, *Nucl. Fusion* **64**, 086049 (2024).

[138] M. Giacomin, D. Kennedy, F. J. Casson, J. Ajay C., D. Dickinson, B. S. Patel, and C. M. Roach, On electromagnetic turbulence and transport in STEP, *Nucl. Fusion* **66**, 055010 (2023).

[139] M. F. Martin, M. Landreman, P. Xanthopoulos, N. R. Mandell, and W. Dorland, The parallel boundary condition for turbulence simulations in low magnetic shear devices, *Plasma Phys. Control. Fusion* **60**, 095008 (2018).